



# Experimental and numerical investigation of the vibro-acoustic behavior of fiber metal laminate

Arul Raj Vaiduriyam<sup>1</sup> · Lenin Babu Mailan Chinnapandi<sup>1,2</sup>

Received: 18 October 2021 / Accepted: 28 April 2022 / Published online: 9 June 2022

© The Author(s), under exclusive licence to The Brazilian Society of Mechanical Sciences and Engineering 2022

## Abstract

This paper discusses in detail the vibration and acoustic characteristics of the glass laminate aluminum-reinforced epoxy (GLARE) hybrid panel with glass fiber-reinforced composite (GFRC) and aluminum. Elastic properties of the plate are obtained using experimental and micromechanics approaches. Reddy's higher-order shear deformation theory is used to analyze the vibro-acoustic characteristics of the GLARE panels. The free vibration characteristics of the GLARE-5 panel were determined using experimental modal analysis and finite element analysis (FEA). Four-noded non-confirming iso-parametric finite element with 8 degree-of-freedom is used to discretize the GLARE panels in FEA. Modal assurance criterion (MAC) is implemented to correlate the results between experimental and simulated approaches. The structural vibration behavior of GLARE panels is obtained using modal superposition approach. Radiated sound power level, sound transmission loss and sound directivity pattern of GLARE panel were examined numerically for material percentage variations, boundary conditions, aspect ratio, thickness aspect ratio and different GLARE grade configurations. The co-relation between experimental and numerical natural frequencies is good. The MAC results indicate close correlation between experimental and FEA. The results suggest that the radiation efficiency of thin GLARE panel did not vary much for all aspect ratios except all side clamped (CCCC) panel with aspect ratio ( $a/b$ ) 2. Results indicate that any GLARE grades might be suggested to choose any GLARE grades, thickness and aspect ratios for enhanced transmission loss except GLARE-4 and GLARE-5. In addition, the combination of low percentage of GFRC with aluminum enhances better vibration and acoustic characteristics. The material percentage and GLARE grade variations studies might be useful to design the hybrid metal fiber laminates for enhanced vibro-acoustic characteristics.

**Keywords** GLARE · Hybrid composite · Higher-order shear deformation theory (HSDT) · Experimental modal analysis · MAC analysis · Vibro-acoustics · Rayleigh integral · Sound power level (SPW) · Sound transmission loss (STL) · Radiation efficiency (RE) · Octave band frequencies

---

Technical Editor: Samuel da Silva.

---

This is only an example.

---

✉ Lenin Babu Mailan Chinnapandi  
Lenin.babu@vit.ac.in

<sup>1</sup> School of Mechanical Engineering, Vellore Institute of Technology, Chennai 600127, Tamil Nadu, India

<sup>2</sup> Electric Vehicles Incubation, Testing and Research Centre, Vellore Institute of Technology, Chennai 600127, Tamil Nadu, India

## 1 Introduction

An increase in demand for high-performance lightweight aircraft structures with high strength has developed a new class of composite materials such as fiber-metal laminate (FML) [1]. A layer-by-layer arrangement of a thin aluminum sheet metal and fiber layer forms FML [2] configuration as shown in Fig. 1. It shows enhanced fatigue, fire retardant, high static and cracks resistant properties than conventional polymer composites. First, FML was successfully designed and developed using thin sheet metals and fiber-based epoxy laminate by Prof. Voorgesang, Delft University of Technology, Netherland. Further, he tested various combinations of FML structures and proved that the Kevlar-based FML shown better heat-resistant properties than others. However,

its compressive strength and fatigue life behaviors are low when compared to other FML. To overcome such disadvantages, a new type of FML (GLARE) was developed by Vlot and Gunnink [3]. Much work has been carried out by many authors on GLARE to understand the impact load behavior, energy absorption, tensile load strength, and fatigue strength through various experimental, numerical, and theoretical approaches. Among them, Holleman [4] has given an overview of selection criteria of aluminum, fiber, adhesive and design guidelines for GLARE composites. After the initial development of FML composites, many researchers have shown key interest in fabricating GLARE panels with various combinations for enhanced mechanical and impact strength.

Sinke [5] has discussed and compared various processes involved in manufacturing and machining of GLARE composite with the conventional sheet metal works. Botelho et al. [6] made a comprehensive study on GLARE composite and how the strength has changed with respect to different types of fibers and their grades. Table 1 shows the different grades and configurations of GLARE panels used in the market are available for commercial purposes. Wu and Yang [7] critically reviewed and listed recent developments in GLARE by considering tensile, compressive, shear, fracture resistance, notched residual strength, impact and environmental durability as key parameters and also pointed out the need for further investigation on GLARE by considering the combined effect of temperature and moisture to understand the damage mechanism and durability and the author also focused on optimizing the material constituents based on the volume fractions of adhesive (Epoxy) with different glass fibers such as R-glass and S-glass from GLARE-1 to GLARE-6 grades. Wilk and Sliwa [8] tested mechanical strength of the GLARE panel by changing the stacking configuration with aluminum 2024, 6061 and 7075 alloys. Based on the literature review, it is evident that the different material grades and layups were used for the fabrication of GLARE panels and impact strength was studied by many researchers.

**Table 1** Standard GLARE grades Botelho et al. [6]

Grade	Sub-grade	Orientation of fiber in each layer
GLARE-1	–	[Al/0°/0°/Al] <sub>s</sub>
GLARE-2	2A	[Al/0°/0°/Al] <sub>s</sub>
	2B	[Al/90°/90°/Al] <sub>s</sub>
GLARE-3	–	[Al/0°/90°/Al] <sub>s</sub>
GLARE-4	4A	[Al/0°/90°/0°/Al] <sub>s</sub>
	4B	[Al/90°/0°/90°/Al] <sub>s</sub>
GLARE-5	–	[Al/0°/90°/90°/0°/Al] <sub>s</sub>
GLARE-6	6A	[Al/+45°/–45°/Al] <sub>s</sub>
	6B	[Al/–45°/+45°/Al] <sub>s</sub>

Alemi-Ardakani and Ghazavi [9] examined glass-fiber-reinforced aluminum to study the effect of bonding adhesion on resistance under low-velocity impact. Sadighi et al. [10] studied various FMLs with different thicknesses and materials for low-velocity impact behavior. In this work, a nonlinear transient finite element analysis was carried out to study the influence of elements on impact strength. Further, the study discusses the selection of finite elements had much more influence than the selection of failure criterion on impact strength results. Hinz et al. [11] analyzed interlaminar shear strength of a composite plate with glass fiber using a representative volume finite element and experimental approaches and developed a new model to simulate de-bonding at the fiber-matrix interface of the interlaminar transverse composite ply. Further, the consequences of de-bonding after interlaminar shear load are also studied in detail.

Material properties extraction plays a significant role in numerical studies. Chen and Cheng [12] investigated the overall elastic behavior of the composite material and thermal expansion coefficients based on a micromechanical approach and compared the results with an experimental study. Chen and Cheng [13] extracted the orthotropic properties of short and continuous glass fiber composite material using an experimental approach. Chen and Sun [14] extracted elastic and plastic properties of an Aramid-reinforced aluminum laminate (ARALL) using a macro-mechanical approach. In this work, researchers used both orthotropic plasticity and laminated plate theories to get the elasto-plastic model. In the first case, a three-parameter plastic potential functions to model the ARALL laminate as a whole and in the second case, distinct linearly elastic and elasto-plastic models were used for aluminum and Kevlar layers. They found that the orthotropic model gave reasonable accurate results up to a total strain of 1.2 percent when compared to the experimental studies. Wang [15] analyzed micromechanics of the fibrous composite materials and developed an analytical model to describe the mechanics of material under external load. Upadhyay and Lyons [16] used a micromechanics-based three-phase model to examine the effective elastic properties of three-phase composites. Further, the effect of inter-phase coating on elastic constants was examined and found the degree of degradation plays a significant role in mechanical properties. Soltani et al. [17] proposed a numerical model to predict the nonlinear behavior of GLARE laminates by using a finite element approach. Tensile properties of reinforced polypropylene-based FML sandwich panels were investigated by Lee et al. [18] using ASTM D-3039 test standards.

Based on the conducted survey, most of the research carried out is focused on the development and testing of the elastic properties of GLARE. Very few discussed their structural behavior under external static and dynamic loads.

Harras [19] investigated the vibration amplitudes of all side clamped (CCCC) GLARE-3 panels by using a nonlinear model and found that the amplitude depends upon the first nonlinear mode shape. They examined the free vibration characteristics such as natural frequencies and bending mode shapes of the GLARE-3 panel using experimental and numerical approaches. Botelho et al. [20] examined free vibration characteristics of FMLs by experimental testing and compared the results with micromechanics-based theoretical calculations. Calculated damping behavior such as storage modulus and loss factors was used to estimate the visco-elastic behavior of hybrid FML. Rahimi et al. [21] examined the effect of boundary conditions and layup directions on free vibration characteristics of an FML annular plate. In vibration testing, modal assurance criterion (MAC) plays a major role in calculating the correlation coefficient between experimental and numerical modal vectors Heylen and Janter [22]. Allemang [23] reviewed the development of the MAC with other related assurance criteria proposed over the last twenty years and demonstrated how a statistical concept is used in structural dynamics application problems. The above works were concentrated only on vibration characteristics of the GLARE panel. However, much works have been carried on the determination of acoustical characteristics (sound radiation, sound transmission loss (STL) and radiation efficiency (RE)) of isotropic, composite and functionally graded material (FGM) panels using experimental, analytical and numerical approaches.

Rayleigh [24] is the pioneer to develop an analytical method to find the acoustic properties of the flat panels resting with baffled conditions. Li and Li [25] studied the effect of mass loading on sound radiation behavior of a plate located at air and water medium. Significant changes were observed in the sound radiation behavior of a mass-loaded panel under air than water. Chandra et al. [26] used analytical methods to study the vibro-acoustic behavior of functionally graded plates. Sharma et al. [27] investigated the vibro-acoustic behavior of shear deformable laminated composite flat panel using boundary element method (BEM) and the higher-order shear deformation theory (HSDT). Arunkumar et al. [28] developed an equivalent model to examine vibro-acoustic characteristics of honeycomb sandwich panel. In their work, ANSYS software and Rayleigh integral approaches were used to get forced vibration response and sound radiation characteristics. Further, Arunkumar et al. [29] extended their approach to study the vibro-acoustic behavior of sandwich panels with truss core filled with foam. In all most of the above works, first-order shear deformation theory (FSDT)-based models were used to study both static and dynamic characteristics of GLARE and composite panels. Doong et al. [30] examined the vibration and stability of pre-stressed cross-ply laminated composite plates using HSDT. Khoa and Thinh [31] used

Reddy's higher-order shear deformation theory based on 4-noded finite elements with seven degrees of freedom to analyze the dynamic behavior of composite panels. Sharma et al. [32] investigated the vibro-acoustic characteristics of the multilayered composite doubly curved shell panel using nine-noded iso-parametric Lagrangian elements with nine degrees of freedom per node.

Sufficient works related to FML were concentrated only on the extraction of mechanical properties, energy absorption, impact and static structural behavior by an experimental and numerical approach. Further, minimal researchers worked with experimental studies to extract the natural frequencies of hybrid FML. However, in this work, the vibro-acoustic behavior of GLARE, such as free, forced vibration characteristics, sound power level, sound transmission loss and radiations efficiency have been examined, along with the effect of boundary conditions (all side clamped-CCCC, all side simply supported-SSSS), aspect ratio ( $a/b = 0.5, 1, 1.5, 2$ ), thickness ratio ( $a/h = 5, 30, 50, 83.33$ ) and material percentage variation from 100 % aluminum to 100 % composite panels using experimental and finite element approaches (HSDT).

## 2 Problem description and methodology

A rectangular GLARE-5 hybrid panel as shown in Fig. 1 with  $[Al/0^\circ/90^\circ/90^\circ/0^\circ/Al]_s$  multilayered configuration is considered for the detailed investigation. It is assumed that the layers of the GLARE panel are perfectly bonded. The complete overview of the methodology followed for the above investigation is given in Fig. 2.

### 2.1 Manufacturing of GLARE-5 composite panel

Traditional hand layup techniques were used to manufacture the GLARE-5 multilayered composite laminate having dimensions of 300 mm  $\times$  215 mm  $\times$  3.58 mm with stacking sequence as shown in Fig. 3a. A commercially available aluminum sheet with 0.18 mm thickness was used for this purpose. The properties of the glass fiber and epoxy resin materials used to make the samples are given in Tables 2 and 3. The aluminum sheet roll is cut into uniform pieces with dimensions equal to the panel's length and width. Similarly, the glass fibers in the form of uni-directional glass fiber were cut according to the panel's length. 92 % of thermosetting polymer epoxy and 8 % of amine-based hardener (curing agent) were mixed in a beaker and uniform stirring is applied with the mechanical stirrer. Hardener addition helps to speed up the curing period of the composite material.

Initially, the flat surface is cleaned and polished with the release gel or wax to avoid composite sticking. Next, the aluminum sheet metal is placed over the flat surface and the prepared resin matrix is poured on the surface of the aluminum

**Fig. 1** GLARE-5 Composite panel

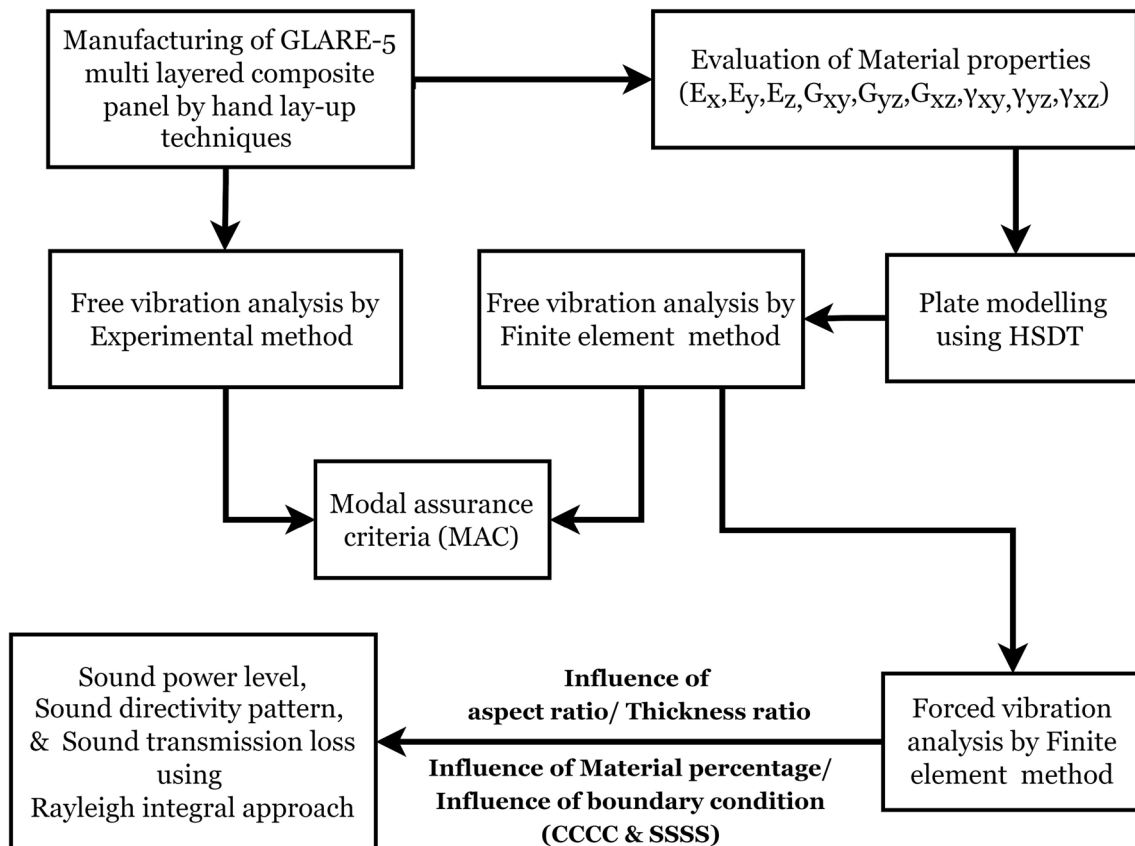
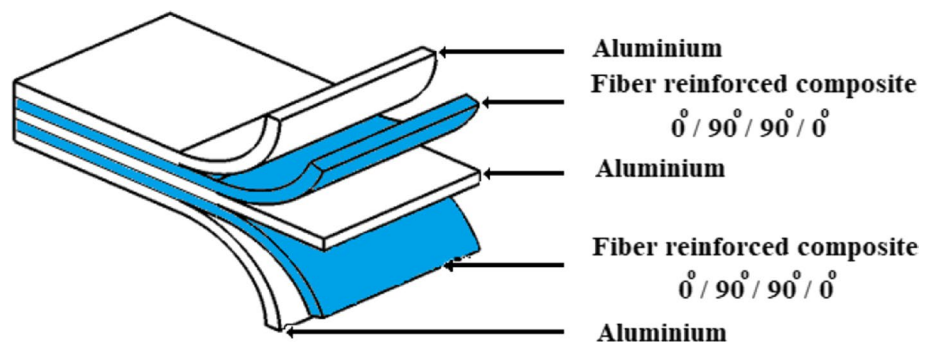


**Fig. 2** Methodology

sheet metal. After ensuring the poured resins spread uniformly throughout the surface, the glass fiber layer is placed on the top of the aluminum sheet and resin. As part of the fabrication process of the composite panel, the unidirectional glass fiber is quenched with epoxy to reduce voids and porosity. [33]. The roller is applied over the glass fiber layer to remove shrinks and excess resins from the surface layer. The same process is continued for all the stacked configurations shown in Fig. 3a. After completing all the layers, a flat plate is placed over the top surface, and a uniform pressure load is applied over the GLARE-5 composite panel by a universal

compression machine as shown in Fig. 4 to decrease the geometry imperfection and to achieve uniform thickness over the cross section of the panel. After a standard curing period of 48-hours at room temperature for epoxy-based polymers, the specimens are used for further studies. The calculated material percentage of aluminum and composite of the fabricated sample were used for further numerical investigation. GLARE-5 panel is prepared with aluminum layers of thickness 0.18 mm and glass/epoxy laminates with  $[0^\circ/90^\circ/90^\circ/0^\circ]$  layup scheme having a thickness of 1.52 mm (each

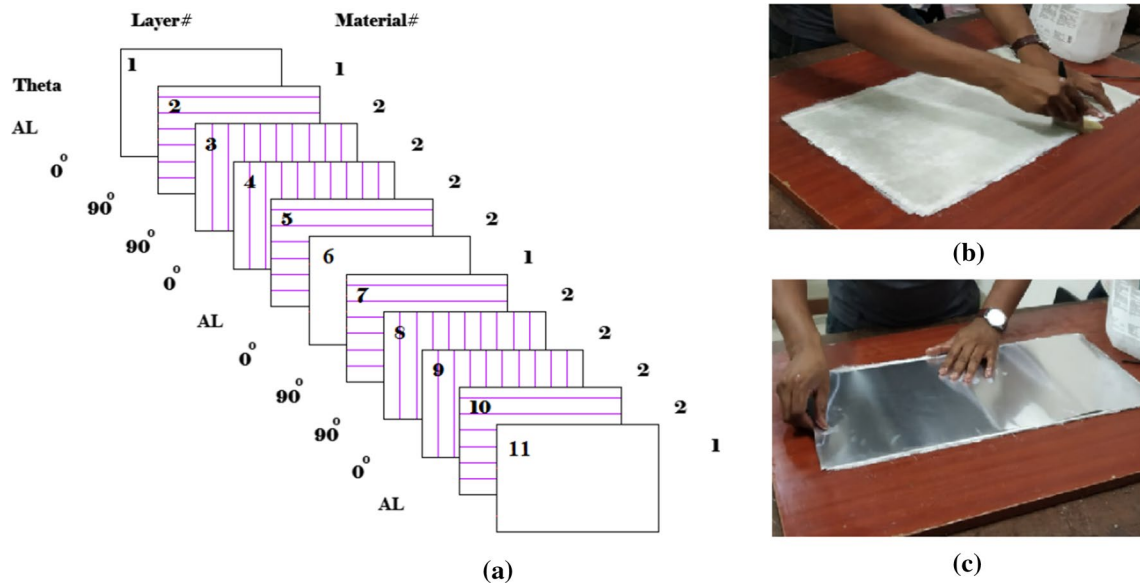


Fig. 3 a Stacking sequence of GLARE-5 composite material, b and c hand layup technique

Table 2 Properties of Epoxy resin

Properties	Value
Density (g/cm <sup>3</sup> )	1.2
Tensile modulus (GPa)	3.5
Epoxy grade	LY556
Curing temperature (°C)	35
Color	White
Amine-based hardener grade	HY951

Table 3 Properties of unidirectional glass fiber

Properties	Value
Density (kg/m <sup>3</sup> )	2620
Diameter of the filament (m)	13 × 10 <sup>-6</sup>
Tensile strength (Pa)	3750 × 10 <sup>6</sup>
Tensile modulus (Pa)	80 × 10 <sup>9</sup>
Elongation (%)	4.8
GSM	500 ± 3 %
Fabric thickness (mm)	0.5 ± 0.03

layer 0.38 mm). The manufactured GLARE panel using the above manufacturing process and microscopic view in thickness directions are shown in Fig. 5a and b.

### 2.2 Evaluation of material properties

Finite element modeling of GLARE-5 laminate requires transverse isotropic properties such as  $E_x, E_y, E_z, G_{xy}, G_{yz},$

$G_{xz}, \gamma_{xy}, \gamma_{yz}, \gamma_{xz}$  [34]. In this study, all elastic properties of the composite material are evaluated using the rule of mixture methods [35, 36]. Table 4 shows the calculated elastic properties using the rule of mixture method.

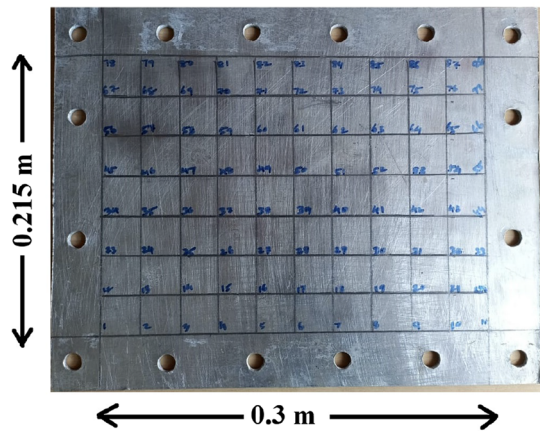
In addition, the obtained Young’s modulus ( $E_x$ ) in fiber direction is verified by performing a standard tensile test using a Universal testing machine. For this purpose, the tensile specimens are individually cut from the manufactured composite plate as per the size mentioned in ASTM D-3039 standard [32] with a length 250 mm, width 25 mm, thickness 3.58 mm, gauge length 150 mm and 50 mm fixing at each end. The test is performed using a universal testing machine INSTRON 8800 under 0.2 mm/min load rate with humidity of 60% and the ambient temperature of 35°C with the clamping pressure of about 10 bar on each side of the test specimen.

### 2.3 Modeling of GLARE-5 laminate using layer wise Reddy’s higher-order shear deformation theory (HSDT)

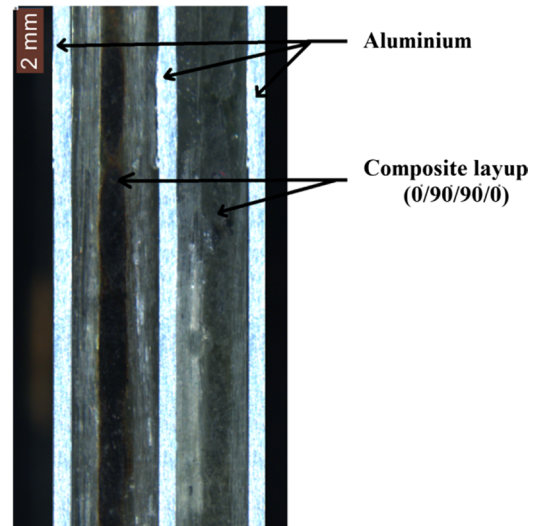
GLARE-5 panel is modeled using Reddy’s layer-wise higher-order shear deformation theory [37] and discretized with 4-noded iso-parametric conforming finite element having eight degrees of freedom per node, namely  $\bar{u}_0, \bar{v}_0, \bar{w}_0, \hat{\phi}_x, \hat{\phi}_y, \frac{\partial \bar{w}_0}{\partial x}, \frac{\partial \bar{w}_0}{\partial y}, \frac{\partial^2 \bar{w}_0}{\partial x \partial y}$ .

Figure 6 shows the layer-wise model of the GLARE-5 composite laminate used for the detailed vibro-acoustic behavior investigation. Figure 7 shows the four-noded iso-parametric elements which are used to discretize the geometry in physical coordinates. The displacement field of the

**Fig. 4** Compression machine for uniform pressure



(a) Manufactured GLARE-5 panel



(b) Microscopic view

**Fig. 5** Manufactured GLARE panel and microscopic view in the thickness direction at 2 mm

**Table 4** Elastic properties of a GLARE-5 composite material

Material	Type	$E_x$ GPa	$E_y$	$E_z$	$G_{xy}$	$G_{yz}$	$G_{zx}$	$\gamma_{xy}$	$\gamma_{yz}$	$\gamma_{zx}$	$\rho$ kg/m <sup>3</sup>
Al	Isotropic	72.39	–	–	–	–	–	0.33	–	–	2700
Glass/epoxy	Transversely isotropic	49.52	11.78	11.78	4.9	4.9	4.9	0.2	0.04	0.04	2058

**Fig. 6** Geometry layup of a GLARE-5 panel

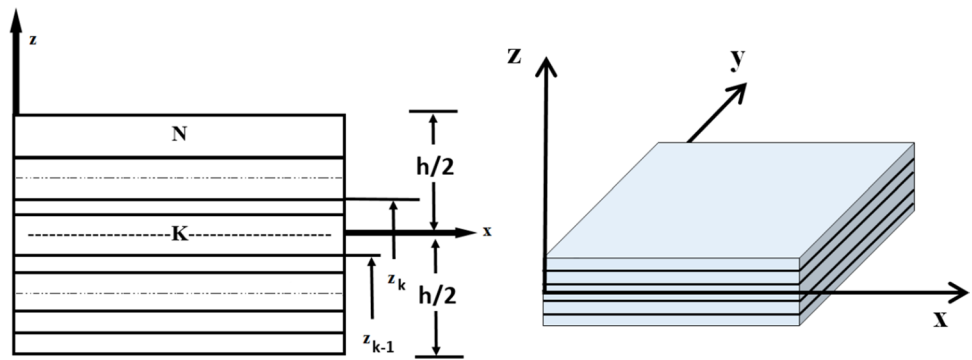
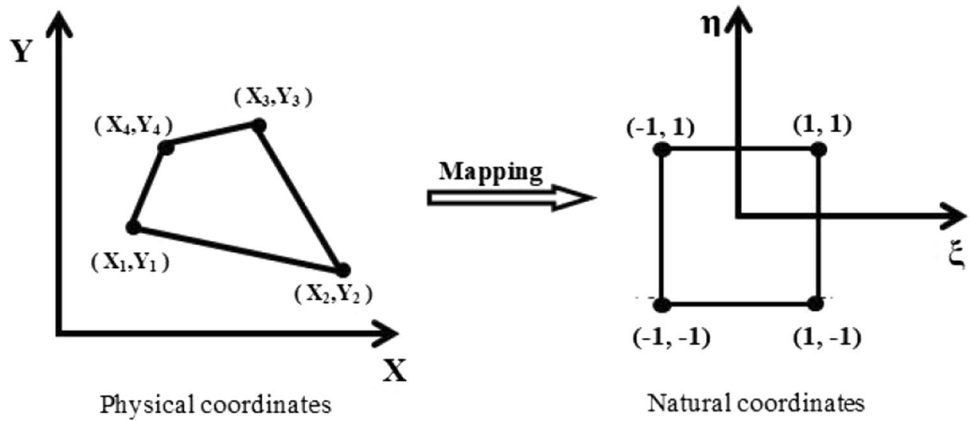


**Fig. 7** Transformation from physical to natural coordinates



GLARE-5 laminated composite panel is given as follows [37]:

$$u = \bar{u}_0 + z\hat{\phi}_x - \frac{4}{3h^2}z^3\left(\hat{\phi}_x + \frac{\partial\bar{w}_0}{\partial x}\right) \quad (1)$$

$$v = \bar{v}_0 + z\hat{\phi}_y - \frac{4}{3h^2}z^3\left(\hat{\phi}_y + \frac{\partial\bar{w}_0}{\partial y}\right) \quad (2)$$

$$w = \bar{w}_0 \quad (3)$$

From Eq. 1, 2 and 3,  $\bar{u}_0 = u_m(x, y, z_0, t)$ ,  $\bar{v}_0 = v_m(x, y, z_0, t)$ ,  $\bar{w}_0 = w_m(x, y, z_0, t)$ ,  $\hat{\phi}_x = \left(\frac{\partial u}{\partial x}\right)_{z=0}$  and  $\hat{\phi}_y = \left(\frac{\partial v}{\partial y}\right)_{z=0}$  are the mid-plane displacements and rotations.

The obtained strain vector using the above displacement is given by,

$$\begin{Bmatrix} \epsilon_{xx} \\ \epsilon_{yy} \\ \gamma_{xy} \\ \gamma_{yz} \\ \gamma_{xz} \end{Bmatrix} = \begin{Bmatrix} \frac{\partial\bar{u}_0}{\partial x} \\ \frac{\partial\bar{v}_0}{\partial y} \\ \frac{\partial\bar{u}_0}{\partial y} + \frac{\partial\bar{v}_0}{\partial x} \\ \phi_y + \frac{\partial\bar{w}_0}{\partial y} \\ \phi_x + \frac{\partial\bar{w}_0}{\partial x} \end{Bmatrix} + z \begin{Bmatrix} \frac{\partial\hat{\phi}_x}{\partial x} \\ \frac{\partial\hat{\phi}_y}{\partial y} \\ \frac{\partial\hat{\phi}_x}{\partial y} + \frac{\partial\hat{\phi}_y}{\partial x} \\ 0 \\ 0 \end{Bmatrix} + z^2 \begin{Bmatrix} 0 \\ 0 \\ 0 \\ \frac{-4}{h^2}\left(\hat{\phi}_y + \frac{\partial\bar{w}_0}{\partial y}\right) \\ \frac{-4}{h^2}\left(\hat{\phi}_x + \frac{\partial\bar{w}_0}{\partial x}\right) \end{Bmatrix} + z^3 \begin{Bmatrix} \frac{-4}{3h^2}\left(\frac{\partial\hat{\phi}_x}{\partial x} + \frac{\partial^2\bar{w}_0}{\partial x^2}\right) \\ \frac{-4}{3h^2}\left(\frac{\partial\hat{\phi}_y}{\partial y} + \frac{\partial^2\bar{w}_0}{\partial y^2}\right) \\ \frac{-4}{3h^2}\left(\frac{\partial\hat{\phi}_x}{\partial y} + \frac{\partial\hat{\phi}_y}{\partial x} + 2\frac{\partial^2\bar{w}_0}{\partial x\partial y}\right) \\ 0 \\ 0 \end{Bmatrix}$$

The generalized strain vector  $\{\varepsilon\}$  of the above equation is given by the relation, Reddy [37],

$$\{\varepsilon\} = \{\varepsilon^0\} + z\{\varepsilon^1\} + z^2\{\varepsilon^2\} + z^3\{\varepsilon^3\} \tag{5}$$

where  $-\gamma_y = \hat{\phi}_y + \frac{\partial \bar{w}_0}{\partial y} \Rightarrow \hat{\phi}_y = -\gamma_y - \frac{\partial \bar{w}_0}{\partial y}$ ,

$$-\gamma_x = \hat{\phi}_x + \frac{\partial \bar{w}_0}{\partial x} \Rightarrow \hat{\phi}_x = -\gamma_x - \frac{\partial \bar{w}_0}{\partial x}, \frac{\partial \hat{\phi}_x}{\partial x} = -\frac{\partial \gamma_x}{\partial x} - \frac{\partial^2 \bar{w}_0}{\partial x^2},$$

$$\frac{\partial \hat{\phi}_y}{\partial y} = -\frac{\partial \gamma_y}{\partial y} - \frac{\partial^2 \bar{w}_0}{\partial y^2}$$

From the above relation,

$$\frac{\partial \hat{\phi}_x}{\partial y} + \frac{\partial \hat{\phi}_y}{\partial x} = -\frac{\partial \gamma_x}{\partial y} - \frac{\partial^2 \bar{w}_0}{\partial x \partial y} - \frac{\partial \gamma_y}{\partial x} - \frac{\partial^2 \bar{w}_0}{\partial x \partial y} \tag{6}$$

$$z \begin{Bmatrix} \frac{\partial \hat{\phi}_x}{\partial x} \\ \frac{\partial \hat{\phi}_y}{\partial y} \\ \frac{\partial \hat{\phi}_x}{\partial y} + \frac{\partial \hat{\phi}_y}{\partial x} \\ 0 \\ 0 \end{Bmatrix} = z \begin{Bmatrix} -\left(\frac{\partial \gamma_x}{\partial x} + \frac{\partial^2 \bar{w}_0}{\partial x^2}\right) \\ -\left(\frac{\partial \gamma_y}{\partial y} + \frac{\partial^2 \bar{w}_0}{\partial y^2}\right) \\ -\left(\frac{\partial \gamma_x}{\partial y} + \frac{\partial \gamma_y}{\partial x} + \frac{2\partial^2 \bar{w}_0}{\partial x \partial y}\right) \\ 0 \\ 0 \end{Bmatrix} \tag{7}$$

$$z^2 \begin{Bmatrix} 0 \\ 0 \\ 0 \\ -\frac{4}{h^2} \left(\hat{\phi}_y + \frac{\partial \bar{w}_0}{\partial y}\right) \\ -\frac{4}{h^2} \left(\hat{\phi}_x + \frac{\partial \bar{w}_0}{\partial x}\right) \end{Bmatrix} = z^2 \begin{Bmatrix} 0 \\ 0 \\ 0 \\ \frac{4}{h^2} \gamma_y \\ \frac{4}{h^2} \gamma_x \end{Bmatrix} \tag{8}$$

$$\left. \begin{Bmatrix} -\left(-\frac{\partial \gamma_x}{\partial x} - \frac{\partial^2 \bar{w}_0}{\partial x^2} + \frac{\partial^2 \bar{w}_0}{\partial x^2}\right) \\ -\left(-\frac{\partial \gamma_y}{\partial y} - \frac{\partial^2 \bar{w}_0}{\partial y^2} + \frac{\partial^2 \bar{w}_0}{\partial y^2}\right) \\ -\left(-\frac{\partial \gamma_x}{\partial y} - \frac{\partial \gamma_y}{\partial x} - 2\frac{\partial^2 \bar{w}_0}{\partial x \partial y} + 2\frac{\partial^2 \bar{w}_0}{\partial x \partial y}\right) \\ 0 \\ 0 \end{Bmatrix} \right\} z^3 \frac{4}{3h^2}$$

$$= z^3 \begin{Bmatrix} \frac{4}{3h^2} \frac{\partial \gamma_x}{\partial x} \\ \frac{4}{3h^2} \frac{\partial \gamma_y}{\partial y} \\ \frac{4}{3h^2} \left(\frac{\partial \gamma_x}{\partial y} + \frac{\partial \gamma_y}{\partial x}\right) \\ 0 \\ 0 \end{Bmatrix} \tag{9}$$

The constitutive equation of the  $k$ th layer is given by

$$\begin{Bmatrix} \sigma_x \\ \sigma_y \\ \sigma_{xy} \\ \sigma_{yz} \\ \sigma_{xz} \end{Bmatrix}_k = \begin{bmatrix} \tilde{C}_{11} & \tilde{C}_{12} & \tilde{C}_{16} & 0 & 0 \\ \tilde{C}_{12} & \tilde{C}_{22} & \tilde{C}_{26} & 0 & 0 \\ \tilde{C}_{16} & \tilde{C}_{26} & \tilde{C}_{66} & 0 & 0 \\ 0 & 0 & 0 & \tilde{C}_{44} & \tilde{C}_{45} \\ 0 & 0 & 0 & \tilde{C}_{45} & \tilde{C}_{55} \end{bmatrix} \begin{Bmatrix} \varepsilon_x \\ \varepsilon_y \\ \gamma_{xy} \\ \gamma_{yz} \\ \gamma_{xz} \end{Bmatrix}_k \tag{10}$$

Elastic constants  $[\tilde{C}_{11}], [\tilde{C}_{12}], [\tilde{C}_{16}], [\tilde{C}_{22}], [\tilde{C}_{26}], [\tilde{C}_{66}], [\tilde{C}_{44}], [\tilde{C}_{45}], [\tilde{C}_{55}]$  can be calculated using the material properties  $(E_x, E_y, E_z, G_{xy}, G_{yz}, G_{zx}, \gamma_{xy}, \gamma_{xz}, \gamma_{yz})$ . For more details, the reader may refer to Reddy [37].

By integrating the stress through the plate thickness, we obtain the generalized force–strain relation by,

$$\begin{Bmatrix} \hat{N}^\circ \\ \hat{M}^\circ \\ \hat{P}^\circ \\ \hat{Q}^\circ \\ \hat{W}^\circ \end{Bmatrix} = \begin{bmatrix} \hat{A}^\circ & \hat{B}^\circ & \hat{E}^\circ & 0 & 0 \\ \hat{B}^\circ & \hat{D}^\circ & \hat{F}^\circ & 0 & 0 \\ \hat{E}^\circ & \hat{F}^\circ & \hat{H}^\circ & 0 & 0 \\ 0 & 0 & 0 & \hat{A}' & \hat{D}' \\ 0 & 0 & 0 & \hat{D}' & \hat{F}' \end{bmatrix} \begin{Bmatrix} \varepsilon^0 \\ \kappa \\ \eta \\ \gamma^0 \\ \xi \end{Bmatrix} \tag{11}$$

The different quantities of the rigidity matrix in Eq. (11) can be derived as follows:

$$\begin{aligned} & (\hat{A}^\circ_{ij} \hat{B}^\circ_{ij} \hat{D}^\circ_{ij} \hat{E}^\circ_{ij} \hat{F}^\circ_{ij} \hat{H}^\circ_{ij}) \\ & = \sum_{k=1}^n \int_{h_{k-1}}^{h_k} (\tilde{C}_{ij})_k (1 \ z \ z^2 \ z^3 \ z^4 \ z^6) dz, i, j = 1, 2, 6 \end{aligned} \tag{12}$$

$$\begin{aligned} & (\hat{A}'_{ij} \hat{D}'_{ij} \hat{F}'_{ij}) \\ & = \sum_{k=1}^n \int_{h_{k-1}}^{h_k} (\tilde{C}_{ij})_k (1 \ z^2 \ z^4) dz, i, j = 4, 5 \end{aligned} \tag{13}$$



### 2.4 Finite element formulation for GLARE-5 panel

The Hamilton’s principle of virtual displacement of a typical GLARE-5 panel finite element is given by weak form of the HSDT-based governing equations [37] as follows:

$$\begin{aligned}
 & \int_{\Omega^e} \{N_{xx}\delta u_{0,x} + N_{xy}(\delta u_{0,y} + \delta v_{0,x}) \\
 & + N_{yy}\delta v_{0,y} + (Q_x - c_2R_x)\delta w_{0,x} \\
 & + (Q_y - c_2R_y)\delta w_{0,y} \\
 & - c_1(P_x\delta w_{0,xx} + P_y\delta w_{0,yy} + 2P_{xy}\delta w_{0,xy}) - q\delta w_0 \\
 & + (Q_x - c_2R_x)\delta\phi_x + (M_x - c_1P_x)\delta\phi_{x,x} \\
 & + (M_{xy} - c_1P_{xy})\delta\phi_{x,y} \\
 & + (Q_y - c_2R_y)\delta\phi_y + (M_{xy} - c_1P_{xy})\delta\phi_{y,x} \\
 & + (M_{yy} - c_1P_y)\delta\phi_{y,y} \\
 & + (I_0\ddot{u}_0 + J_1\ddot{\phi}_x - c_1I_3\dot{w}_{0,x})\delta u_0 \\
 & + (I_0\ddot{v}_0 + J_1\ddot{\phi}_y - c_1I_3\dot{w}_{0,y})\delta v_0 \\
 & + (J_1\ddot{u}_0 + K_2\ddot{\phi}_x - c_1J_4\dot{w}_{0,x})\delta\phi_x \\
 & + (J_1\ddot{v}_0 + K_2\ddot{\phi}_y - c_1J_4\dot{w}_{0,y})\delta\phi_y + I_0\ddot{w}_0\delta w_0 \\
 & + c_1(-I_3\ddot{u}_0 - J_4\ddot{\phi}_x + c_1I_6\dot{w}_{0,x})\delta w_{0,x} \\
 & + c_1(-I_3\ddot{v}_0 - J_4\ddot{\phi}_y + c_1I_6\dot{w}_{0,y})\delta w_{0,y} \\
 & + (N_{xx}\hat{w}_{0,x} + N_{xy}\hat{w}_{0,y})\delta w_{0,y} \\
 & + (N_{xy}\hat{w}_{0,x} + N_{yy}\hat{w}_{0,y})\delta w_{0,y} dx dy \} \\
 & - \oint_{\Gamma^e} (N_n\delta u_n + N_{nx}\delta u_{ns}) ds \\
 & - \oint_{\Gamma^e} (\bar{V}_n\delta w_0 + P_{nm}\delta w_{0,n}) ds \\
 & - \oint_{\Gamma^e} (M_n\delta\phi_n + M_{ns}\delta\phi_{ns}) ds = 0
 \end{aligned} \tag{14}$$

A comma followed by subscripts denotes differentiation with respect to the subscripts.  $(N_{xx}, N_{yy}, N_{xy})$  denotes the force resultant,  $(M_{xx}, M_{yy}, M_{xy})$  represent the moment resultants,  $(Q_x$  and  $Q_y)$  are the transverse shear force resultants,  $\delta u_0, \delta v_0, \delta w_0$  are the generalized displacements,  $I_i$  represent mass moment of inertia and it is given by Eqs. 15 and 16, whereas two points above a variable mean the second derivative with respect to time.

$$I_i = \sum_{k=1}^N \int_{z_k}^{z_{k+1}} \rho^{(k)}(z)^i dz (i = 0, 1, 2, \dots, 6) \tag{15}$$

$$\begin{aligned}
 c_1 &= \frac{4}{3h^2}, c_2 = \frac{4}{h^2}, J_i = I_i - c_1I_{i+2}, \\
 K_2 &= I_2 - 2c_1I_4 + c_1^2I_6
 \end{aligned} \tag{16}$$

The generalized displacement is approximated over an element  $\Omega^e$  by the expressions [37].

$$\begin{aligned}
 u_0(x, y, t) &= \sum_{i=1}^N [N_i(x, y)]u_i(t) \\
 v_0(x, y, t) &= \sum_{i=1}^N [N_i(x, y)]v_i(t) \\
 w_0(x, y, t) &= \sum_{i=1}^N [\bar{\Delta}_i(x, y)]\bar{\varphi}_i(t) \\
 \hat{\phi}_x(x, y, t) &= \sum_{i=1}^N [N_i(x, y)]\hat{\phi}_{xi}(t) \\
 \hat{\phi}_y(x, y, t) &= \sum_{i=1}^N [N_i(x, y)]\hat{\phi}_{yi}(t)
 \end{aligned} \tag{17}$$

The constants,  $\bar{\Delta}_i = w_0, \frac{\partial \bar{w}_0}{\partial x}, \frac{\partial \bar{w}_0}{\partial y}, \frac{\partial^2 \bar{w}_0}{\partial x \partial y}, N_i$  and  $\bar{\Delta}_i$  denote Lagrangian and Hermite interpolation functions. The weak form of equations are discretized using the 4-noded isoparametric finite element with 8 DOF per node.

$$\begin{aligned}
 & \begin{bmatrix} [\bar{K}^{11}] & [\bar{K}^{12}] & [\bar{K}^{13}] & [\bar{K}^{14}] & [\bar{K}^{15}] \\ [\bar{K}^{12}]^T & [\bar{K}^{22}] & [\bar{K}^{23}] & [\bar{K}^{24}] & [\bar{K}^{25}] \\ [\bar{K}^{13}]^T & [\bar{K}^{23}]^T & [\bar{K}^{33}] & [\bar{K}^{34}] & [\bar{K}^{35}] \\ [\bar{K}^{14}]^T & [\bar{K}^{24}]^T & [\bar{K}^{34}]^T & [\bar{K}^{44}] & [\bar{K}^{45}] \\ [\bar{K}^{15}]^T & [\bar{K}^{25}]^T & [\bar{K}^{35}]^T & [\bar{K}^{45}]^T & [\bar{K}^{55}] \end{bmatrix} \begin{Bmatrix} u^i \\ v^i \\ \varphi^i \\ \hat{\phi}_x^i \\ \hat{\phi}_y^i \end{Bmatrix} \\
 & + \begin{bmatrix} [\bar{M}^{11}] & [\bar{M}^{12}] & [\bar{M}^{13}] & [\bar{M}^{14}] & [\bar{M}^{15}] \\ [\bar{M}^{12}] & [\bar{M}^{22}] & [\bar{M}^{23}] & [\bar{M}^{24}] & [\bar{M}^{25}] \\ [\bar{M}^{13}]^T & [\bar{M}^{23}]^T & [\bar{M}^{33}] & [\bar{M}^{34}] & [\bar{M}^{35}] \\ [\bar{M}^{14}]^T & [\bar{M}^{24}]^T & [\bar{M}^{34}]^T & [\bar{M}^{44}] & [\bar{M}^{45}] \\ [\bar{M}^{15}] & [\bar{M}^{25}]^T & [\bar{M}^{35}]^T & [\bar{M}^{45}] & [\bar{M}^{55}] \end{bmatrix} \begin{Bmatrix} \ddot{u}^i \\ \ddot{v}^i \\ \ddot{\varphi}^i \\ \ddot{\phi}_x^i \\ \ddot{\phi}_y^i \end{Bmatrix} \\
 & = \begin{Bmatrix} \bar{F}^1 \\ \bar{F}^2 \\ \bar{F}^3 \\ \bar{F}^4 \\ \bar{F}^5 \end{Bmatrix}
 \end{aligned} \tag{18}$$

The functions can be determined using  $\alpha = 1, 2, 3, 4, 5; \Delta_j^1 = u_j; i = 1$  to  $\alpha$ . The complete details of stiffness and mass matrices elements are given in “Appendix”.

### 2.5 Free vibration analysis: numerical approach

Transversely isotropic properties obtained from the micro-mechanics approach in Sect. 2.2 are used to get the stiffness and mass matrices from Eq. (18) with harmonic time dependence assumption. Then, the standard eigenvalue problem is formulated as given in Eq. (19) and solved using MATLAB to get the natural frequencies and mode shapes

$$([\bar{K}] - \omega^2[\bar{M}])X = 0 \tag{19}$$

as per the above equation  $[\bar{K}]$  &  $[\bar{M}]$  is given as the global assembled stiffness and mass matrices of the GLARE panel.

## 2.6 Free vibration analysis: experimental method

Experimental modal analysis is carried out to get the natural frequencies and mode shapes of the panel. A simple laboratory-scale experiment was developed for this purpose using the available vibration fixture and impact hammer test setup. A GLARE-5 panel is fabricated as per the fabrication process specified in Sect. 2.1 with dimensions specified in Fig. 5a. The GLARE-5 panel is clamped over all four sides to arrest all the degrees of freedom using lock nuts with uniform pressure as shown in Fig. 8.

The GLARE-5 panel is excited using Dytron make impulse hammer and the response is measured using a uni-axial accelerometer. The sensitivities of the impact hammer and accelerometer are 10.29 mV/lbf and 104.11 mV/g. In order to avoid nodal locations, the accelerometer is fixed at one by fourth locations of the plate. The accelerometer is mounted on the panel's top surface using a thermo-set adhesive and connected to the M+P VibPilot 8-channel data acquisition system. During the multipoint modal test, one can perform the test by moving the impact hammer or accelerometer between measurement points. But there are some difficulties in moving the accelerometer when making measurements such as changing the position of the accelerometer at the measurement points. Instead, roving the impact hammer to the measuring points will help to overcome the

above difficulties. In addition, roving the accelerometer also alters the mass distribution of the structure, which affect the system natural frequencies. The time taken for a roving hammer is also very less compared to the roving accelerometer. Hence, the roving hammer technique is widely preferable than moving the accelerometer. For the above reasons, the roving hammer technique is used in this work to obtain the natural frequencies and mode shapes of the GLARE-5 panel and the schematic diagram for position of the accelerometer and position of the impact hammer is also shown in Fig. 9. The entire GLARE-5 panel is discretized with  $11 \times 8$  mesh size and excited by the roving hammer method shown in Fig. 9b. The output response is recorded using M+P international software. The recorded time-domain signal is converted into the frequency domain using Fast Fourier Transform (FFT) and operating deflection shape (ODS) analysis is also carried out. Figure 8 shows the GLARE-5 panel, specimen holder and vibration measurement instruments used for free vibration testing.

## 2.7 Modal assurance criterion (MAC)

Modal assurance criterion (MAC) plays an important role in pairing the obtained data from experimental and numerical approaches. This allows us to compare the measured vibration mode shape with the finite element results. The degree of similarity between the two different displacement vectors is expressed in Eq. (20). In general, MAC varies from zero to one (0 to 1) and the MAC value close to zero represents

**Fig. 8** Experimental test setup for free vibration of GLARE-5 panel for all side clamped boundary condition



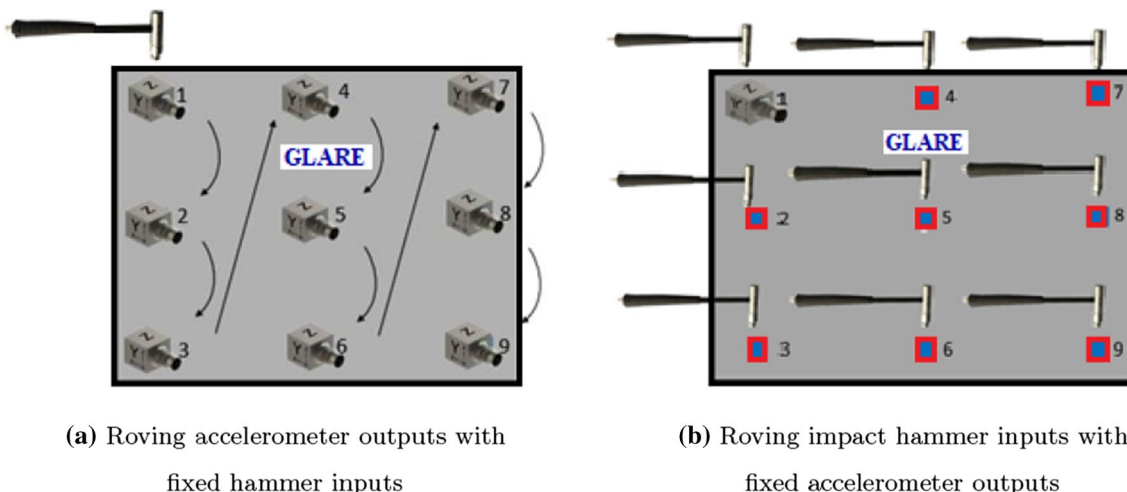


Fig. 9 Schematic diagram for roving accelerometer and roving impact hammer

significant variation between the displacement vectors and the MAC value close to one represents identical shape correlation between displacement vectors. Achieving MAC value exactly equal to one is difficult for most of the cases and the MAC value will always be  $< 1$  [38].

$$MAC(r, q) = \frac{|\{\tilde{\psi}_A\}_r^T \{\tilde{\psi}_X\}_q^*|^2}{(\{\tilde{\psi}_A\}_r^T \{\tilde{\psi}_A\}_r^* \{\tilde{\psi}_X\}_q^T \{\tilde{\psi}_X\}_q^*)} \quad (20)$$

as per the equation for any,  $\{\tilde{\psi}_A\}_r$  is the displacement vector of solution  $A_r$ ,  $\{\tilde{\psi}_A\}_r^T$  is the transpose displacement vector  $\{\tilde{\psi}_A\}_r$ ,  $\{\tilde{\psi}_X\}_q^*$  is the complex conjugate of  $\{\tilde{\psi}_X\}_q$ ,  $\{\tilde{\psi}_X\}_q^T$  is the transpose displacement vector  $\{\tilde{\psi}_X\}_q$  and  $\{\tilde{\psi}_A\}_r^*$  is the complex conjugate of  $\{\tilde{\psi}_A\}_r$ .

### 2.8 Forced vibration analysis using finite element approach

The modal superposition method (MSP) is implemented to estimate the forced vibration response analysis of a GLARE-5 multilayered composite panel [39] by applying a harmonic point load with a magnitude of 1N at the locations 0.5 X, 0.5 Y and 0.75 X, 0.75 Y along in z-direction. The MSP is a unique method for obtaining stable dynamic responses under dynamic loading conditions with high-performance computing efficiencies and low calculation time. The eigenvalues and eigenvectors obtained by solving the standard eigenvalue Eq. (19) were used to perform the forced vibration response of the GLARE-5 panel [40]. The governing equation of motion for a dynamic system acted on by external load is expressed as follows:

$$[\bar{M}_{ij}] \{\ddot{X}\} + [\tilde{C}_{ij}] \{\dot{X}\} + [\bar{K}_{ij}] \{X\} = \bar{F}(t) \quad (21)$$

The function,  $\bar{F}(t)$  is the time-dependent applied force vector and  $\{X\}$  is the displacement vector. The displacement vector in terms of modal coordinates is given by

$$\{X\} = \sum_{k=1}^n [\bar{\phi}] Z_k \quad (22)$$

Thus, the constant,  $\bar{\phi}$  is the ortho-normalized eigenvector as given by the following equation,

$$\bar{\phi} = \frac{1}{\sqrt{\phi_i^T \bar{M}_{ij} \phi_i}} \phi_i \quad (23)$$

i.e.,  $\phi_i$  is the eigenvector and  $\bar{M}_{ij}$  is the mass matrix

$$[\bar{M}_{ij}] [\bar{\phi}] \{\ddot{Z}\} + [\tilde{C}_{ij}] [\bar{\phi}] \{\dot{Z}\} + [\bar{K}_{ij}] [\bar{\phi}] \{Z\} = \bar{F}(t) \quad (24)$$

Pre-multiplying Eq. (24) by  $[\bar{\phi}]^T$  and considering orthogonality condition, the uncoupled equation in modal coordinate is given by

$$\ddot{Z}_k + 2\zeta\omega_n\dot{Z}_k + \omega_k^2 Z_k = \bar{F}_k \quad (25)$$

for,  $k = 1, 2, \dots, n$  (represents mode). For harmonic oscillation, the above equation given by

$$\{Z\}_k = \frac{\bar{F}_k}{(\omega_k^2 - \Omega^2) + 2\zeta\omega_k\Omega} \quad (26)$$

and the actual displacement vector is calculated using Eq. (22)

The surface normal velocity of the GLARE panel is calculated from the vibration displacement response using the following relation

$$\dot{w} = j\omega\{X\} \tag{27}$$

In the above equation,  $\dot{w}$  denotes the surface normal velocity,  $\omega$  represents excitation frequency, and  $\{X\}$  indicates the displacement vector. Then, the average RMS velocity of the GLARE panel is calculated for each frequency using the relation given below

$$V_{RMS} = \sqrt{\frac{1}{N} \sum_{n=1}^N |\dot{w}|^2} \tag{28}$$

### 2.9 Acoustic studies of GLARE-5 panel

Acoustic characteristics such as sound power level (SPL), sound transmission loss (STL), radiation efficiency and sound directivity pattern are obtained from the surface normal velocity of the GLARE panel using the methodology described below.

1. The complex sound pressure at any point can be obtained in terms of the plate surface normal velocity using the Rayleigh integral as given below

Complex pressure amplitude  $\bar{p}(\bar{r})$

$$= \frac{j\rho ck}{2\pi} \int_S \dot{w}(r_s) \frac{e^{-jk|\bar{r}-\bar{r}_s|}}{|\bar{r}-\bar{r}_s|} ds \tag{29}$$

The constant,  $\rho$  is the density of the air medium,  $c$  is the velocity of sound,  $S$  is the surface area of the plate,  $\bar{r}_s$  is the point located on the surface  $S$ ,  $\bar{r}$  is the field point,  $\dot{w}(\bar{r}_s)$  is the surface normal velocity,  $|\bar{r}-\bar{r}_s|$  is the distance between a surface point and the field point,  $k$  is the wave number ( $k = \omega/c$ ) and  $\omega$  is the circular frequency. Figure 10 shows the geometric interpretation of the sound pressure calculation at any point above the vibrating panel.

$$\bar{W} = \frac{1}{2} Re \left( \oint \bar{p}(\bar{r}) \dot{w}^*(\bar{r}) \right) ds \tag{30}$$

where  $\bar{W}$  is the sound power,  $\bar{p}(\bar{r})$  is the complex pressure amplitude, and  $\dot{w}^*(\bar{r})$  is the complex conjugate of the acoustic particle velocity. Then, the sound power level can be calculated using the equation as follows:

$$\text{Sound power level (SPWL)} = 10 \log \frac{\bar{W}}{\bar{W}_{ref}} \tag{31}$$

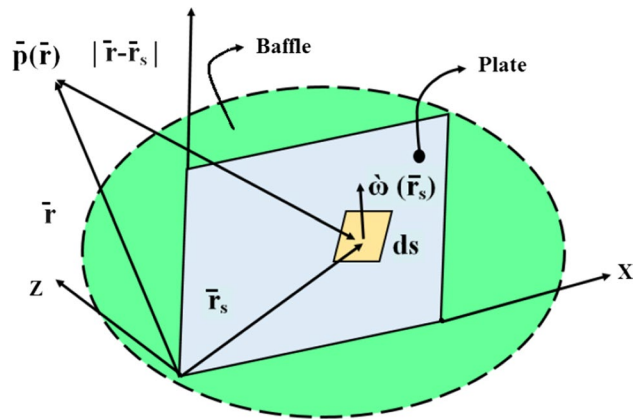


Fig. 10 Geometric interpretation of the panel

- where  $\hat{W}_{ref}$  represents the reference power ( $\hat{W}_{ref} = 1 \times 10^{-12} \text{ Watts}$ )
2. Radiation efficiency of the vibrating panel can be calculated using equation

$$\sigma = \frac{\bar{W}}{\rho c S V^2} \tag{32}$$

From the above equation,  $V^2 = \dot{V}_n^H N \dot{V}_n$ ,  $V$  is the spatial time averaged normal velocity,  $N = (1/2N)\mathbf{I}$ ,  $N$  is the number of elements used in the discretization,  $\mathbf{I}$  is the identity matrix and  $\bar{W}$  is the sound power taken from the Eq. (30)

3. Using the Rayleigh integral approach, the sound pressure at a field point is given in terms of surface velocity by the following equation,

$$\bar{p}(\bar{r}, \theta) = \frac{j\rho\omega}{2\pi} \int_{-L/2}^{L/2} \int_{-W/2}^{W/2} \dot{w}(x, y) \frac{e^{-jk|\bar{r}-\bar{r}_s|}}{|\bar{r}-\bar{r}_s|} dx dy \tag{33}$$

In the above equation,  $|\bar{r}-\bar{r}_s|$  is the distance between a surface point and the field point,  $\dot{w}(x, y)$  is the acoustic particle velocity,  $\bar{r}$  is the field point,  $\bar{r}_s$  is the point located on the surface  $S$ .

Sound pressure at a distance of 1m from the center of the panel is calculated using the above relation by varying the angles from  $0^\circ$  to  $180^\circ$  and it is shown in Fig. 11.

Then, the sound pressure level is calculated at field points by the equation given below

$$\text{SPL} = 20 \log \frac{\bar{p}}{\bar{p}_{ref}} \tag{34}$$

4. Transmission loss is defined as the ratio of incoming and transmitted sound power. The sound transmission loss of the GLARE-5 panel in decibel is given by Eq. (35)

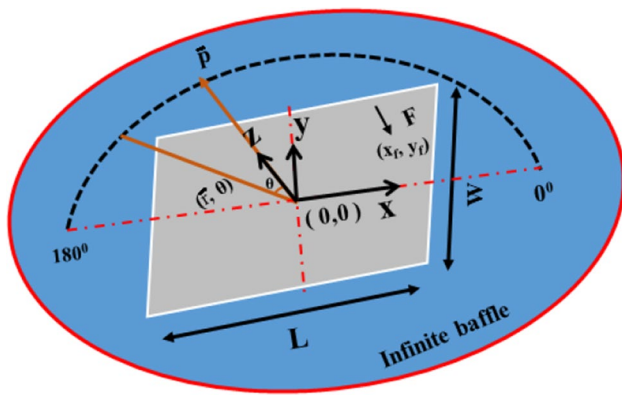


Fig. 11 A baffled rectangular panel with the main geometrical parameters and defined coordinate systems

$$STL = 10 \log_{10} \frac{1}{\tau} \tag{35}$$

The function  $\tau$  represents the transmission ratio which is defined as the ratio of transmitted power ( $\bar{W}$ ) and incident power ( $W_i$ ) and it is given by,

$$\tau = \frac{\bar{W}}{W_i} \tag{36}$$

The constant, transmitted sound power ( $\bar{W}$ ) is calculated from Eq. 30 and incident sound power ( $W_i = p_i^2 \cos \theta LW / 2\rho c$ ),  $p_i$  is incident pressure assumed to be a real constant ( $1N/m^2$ ),  $\theta$  is normal incidence angle ( $\theta = 0^\circ$ ) in radian, L is the length, W refers to width of the GLARE-5 panel, respectively, and the reader may also refer to [26, 41] for further details.

### 3 Validation studies

#### 3.1 Validation of Reddy’s higher-order shear deformation theory

In order to verify the developed finite element model, a simply supported square 4-layered laminated composite plate [0°/90°/90°/0°] was analyzed by Peng [42] is considered for validation. The material properties of the composite layer are given by Peng [42] as  $E_1 = 175 \times 10^9$  Pa,  $E_2 = 7 \times 10^9$  Pa,  $G_{12} = G_{13} = 3.5 \times 10^9$  Pa,  $G_{23} = 1.4 \times 10^9$  Pa,  $\gamma_{12} = \gamma_{13} = 0.25$ .

Table 5 shows the results of proposed model and Peng [42] for bending deflection and stress variations. It shows good agreement between the two and the present HSDT-based finite element model predicts the bending deflection more accurately.

Table 5 Non-dimensionalized deflection and stresses in simply supported condition for symmetric cross-ply squared laminates

$a/h = 4, a/b = 1$		0°/90°/90°/0° Symmetric cross-ply squared laminates			
		$\sigma_{xz}$		$\sigma_{xy}$	
$\bar{w} \times 10^2$					
Peng [42]	1.894	Present HSDT	0.632	Present HSDT	0.206
		Peng [42]	0.632	Peng [42]	0.206
		Present HSDT	0.6755	Present HSDT	0.2109
		Peng [42]	0.665	Peng [42]	0.0444
		Present HSDT	1.9144	Present HSDT	0.0333

### 3.2 Validation of sound power level

Similarly to verify the developed Rayleigh integral code, a simply supported rectangular isotropic plate with the dimensions of  $0.445 \text{ m} \times 0.379 \text{ m} \times 0.003 \text{ m}$ , was analyzed by Li and Li [25] for radiated sound power level which is considered for the material properties of the isotropic plate given [25] as density  $\rho = 7850 \text{ kg/m}^3$ , Young's modulus  $E = 2.1 \times 10^{11} \text{ N/m}^2$ , and Poisson's ratio  $\gamma = 0.3$ , is taken for validation. The plate is assumed to be vibrating in air medium with density and sound speed of about  $\rho = 1.21 \text{ kg/m}^3$ ,  $c = 343 \text{ m/s}$ . The isotropic plate is modeled using Reddy's HSDT theory and discretized with a 4-noded finite element. The sound power level of the vibrating surface is computed by exciting the isotropic plate by a harmonic load with 1N magnitude ( $F e^{j\omega t}$ ) along normal to the thickness. Figure 12 shows the comparison of radiated sound power level and good agreement between the two.

## 4 Results and discussion

GLARE-5 hybrid multilayered composite plate having dimensions of 0.3 m and 0.215 m along length and width directions is considered for the detailed investigation of vibro-acoustic behavior using experimental and HSDT based finite element methods. The influence of aspect ratio, boundary conditions, thickness ratio and material percentage variation on vibro-acoustic behavior of GLARE-5 composite plate is examined in detail. The material properties of aluminum and glass fiber/epoxy used for the detailed investigation are given in Table 4. The thickness of aluminum and glass/epoxy laminates with  $[0^\circ/90^\circ/90^\circ/0^\circ]$  layup is 0.18 mm and 1.52 mm. It is assumed that the plate is vibrating in air medium and discretized using a 4-noded HSDT-based finite element with eight degrees of freedom (DOF) per node. The detailed convergence study has been carried out

for the highest natural frequency considered for the analysis, and the results are compared with the experimental natural frequencies.

Next, the vibration displacement response of the plate is obtained by applying a harmonic point load at a distance of about 0.75 length and 0.75 width from the origin of the panel. Then, the Rayleigh integral is used to obtain the acoustic response using the obtained displacement response for each frequency. Vibro-acoustic quantities such as displacement, velocity and root mean square (RMS) acceleration at the driving point, radiated sound power, sound pressure level, overall sound power level and sound transmission loss are computed using Eqs. (29)–(35).

### 4.1 Modal analysis

Modal analysis is carried out on the GLARE-5 panel using HSDT-based finite element method and experimental methods as shown in Fig. 8 and described in Sects. 2.5 and 2.6. A converged finite element mesh size of  $11 \times 11$  is used to obtain the natural frequencies and eigenvectors by solving Eq. (19). Extracted natural frequencies from the experimental modal analysis are compared with the finite element results. Table 6 shows the comparison of the first five natural

**Table 6** Natural frequencies of GLARE-5 panel by experimental and present finite element approach (HSDT)

Modal indices	Experiment	HSDT-based finite element method	Error%
(1,1)	428.90	430.54	0.38
(2,1)	678.12	702.84	3.52
(1,2)	1048.41	1028.71	- 1.91
(3,1)	1172.63	1171.45	- 0.09
(2,2)	1273.45	1252.02	- 1.70

**Fig. 12** Present study of sound power level with Li and Li [25]

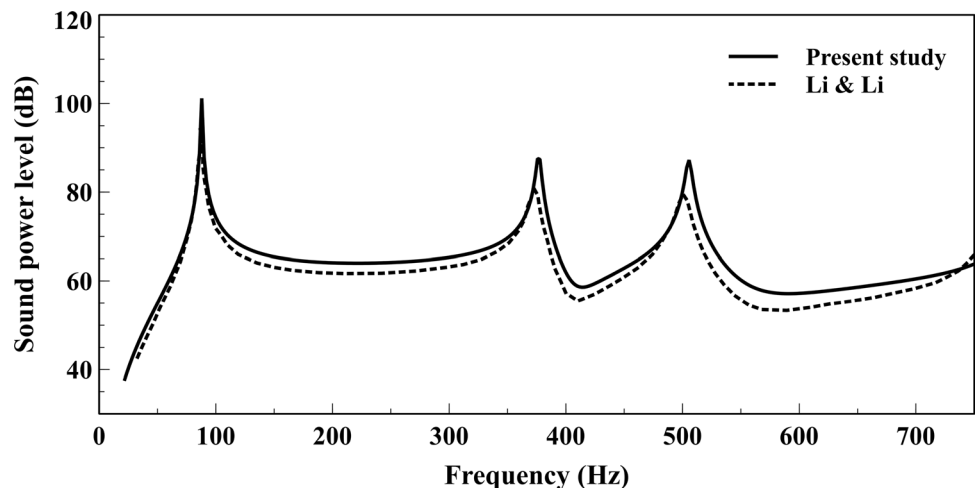


**Table 7** Modal assurance criterion (MAC) for CCCC boundary condition

MAC	Experimental frequency (Hz)				
	428.90	678.12	1048.41	1172.63	1273.45
<i>Numerical frequency (Hz)</i>					
<b>430.54</b>	<b>0.93</b>	0.06	0.06	0.02	0.05
<b>702.84</b>	0.04	<b>0.92</b>	0.07	0.09	0.06
<b>1028.71</b>	0.05	0.04	<b>0.92</b>	0.08	0.06
<b>1171.45</b>	0.05	0.05	0.01	<b>0.81</b>	0.01
<b>1252.02</b>	0.07	0.07	0.05	0.09	<b>0.90</b>

Bold highlighted diagonal values represent the modal assurance criterion (MAC) which indicate the similarity between the experimental and numerical results

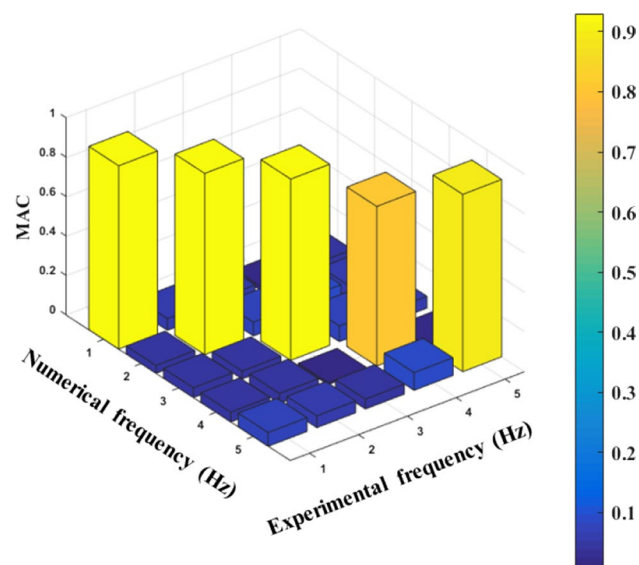


**Fig. 13** MAC comparison between experimental and numerical results

frequencies extracted from experimental and finite element methods along with the percentage of error. From Table 6, it is clear that the obtained natural frequencies using the experimental method are closely matching with numerical results for the selected modes with less percentage of errors.

The extracted experimental natural frequencies were verified with numerical results by MAC analysis according to the procedure described in Sect. 2.7. For this purpose, an in-house MATLAB code has been developed to compare the displacements extracted from the ODS analysis with the numerical results for each frequency. Calculated MAC values are listed in Table 7, and it clearly shows that the diagonal values are nearly equal to one and the mode shapes are perfectly matched to each other. The compared MAC values are plotted with the help of a confusion matrix plot in 3-D as shown in Fig. 13.

### 4.2 Influence of load location on vibro-acoustic behavior

To examine, how the modes have been shifted based on the loading condition, a GLARE-5 panel with dimensions specified in Sect. 2.1 is considered for detailed investigation on vibro-acoustic behavior due to excitation locations. For this purpose, a harmonic load is applied at center and offset locations with 1N magnitude in the frequency range from 1 Hz to 2500 Hz. The forced vibration response and RMS velocity of the GLARE-5 panel are calculated using the modal superposition method as specified in Sect. 2.8 and the radiated sound power level of the panel is calculated as specified in Sect. 2.9. Figures 14 and 15 show the results of sound power level and average RMS velocity due to center and offset locations.

From Fig. 14, it is clear that when the load is acting at the center of the panel, few modes were not excited due to the position of excitation location nearer to panels nodal

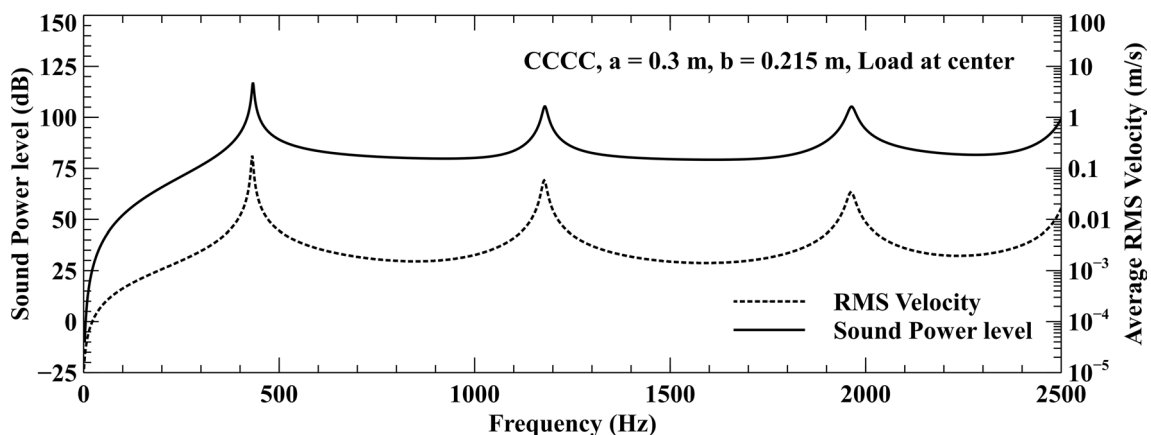


**Fig. 14** Effect of sound power level and RMS velocity for load acting at center

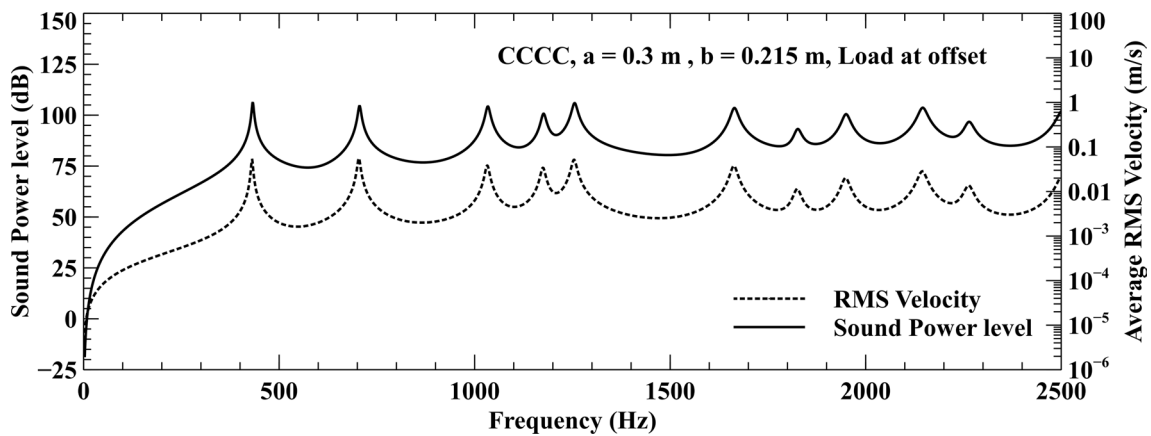


Fig. 15 Effect of sound power level and RMS velocity for load acting at offset distance

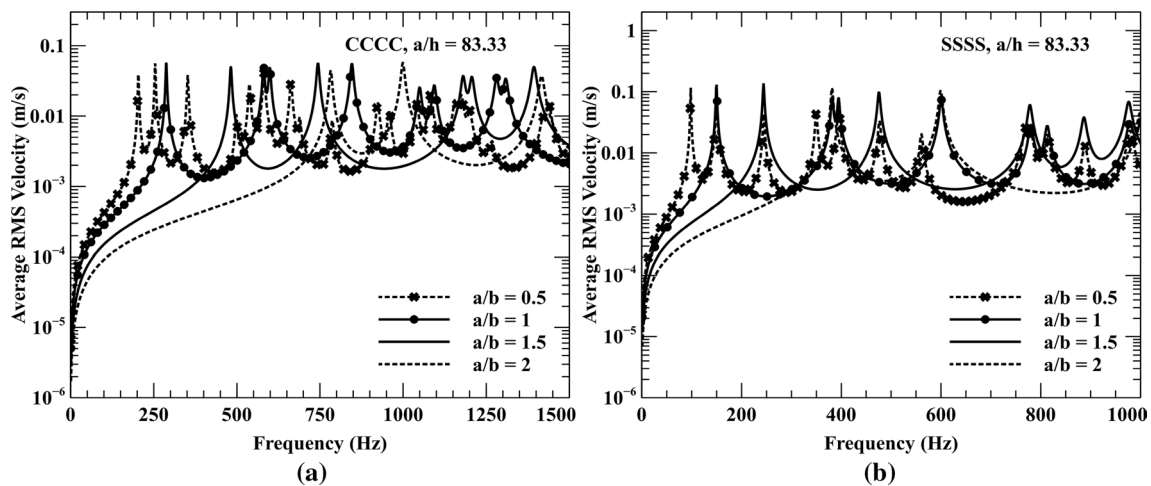


Fig. 16 Effect of average RMS velocity for different aspect ratio and boundary conditions

positions corresponds to the particular mode. The entire modes between the selected frequency range are observed when the load is shifted from center to offset location as seen in Fig. 15. Both average RMS velocity and sound power level are overlaid for the load acting at the center and offset locations on a single plot to show how the peak amplitude matches each other at natural frequencies.

### 4.3 Influence of aspect ratio and boundary conditions on vibro-acoustic behavior

The influence of aspect ratio ( $a/b$ ) on vibro-acoustic characteristics of GLARE panel is analyzed for all side clamped (CCCC) and simply supported (SSSS) boundary conditions. Table 8 shows the extracted natural frequencies for different aspect ratios using the finite element method. The results show that the natural frequencies increase as the aspect ratio increases for all sides clamped and simply supported

Table 8 Modal frequencies for different aspect ratio and boundary condition

Boundary conditions	Modal frequencies of GLARE-5 panel				
	Mode	$a/b = 0.5$	$a/b = 1$	$a/b = 1.5$	$a/b = 2$
CCCC $a/h = 83.33$	1	204.41	288.26	482.67	783.11
	2	254.96	580.72	745.63	999.91
	3	352.79	599.40	1184.00	1416.90
	4	498.71	846.69	1210.50	2033.90
	5	538.28	1050.30	1396.80	2048.30
	6	582.11	1094.30	1792.70	2228.70
SSSS $a/h = 83.33$	1	98.88	150.52	244.89	382.09
	2	150.65	382.51	476.49	600.11
	3	245.43	395.20	778.92	999.39
	4	350.49	601.15	887.20	1341.51
	5	382.71	780.72	976.87	1526.52
	6	395.42	813.73	1345.90	1577.00



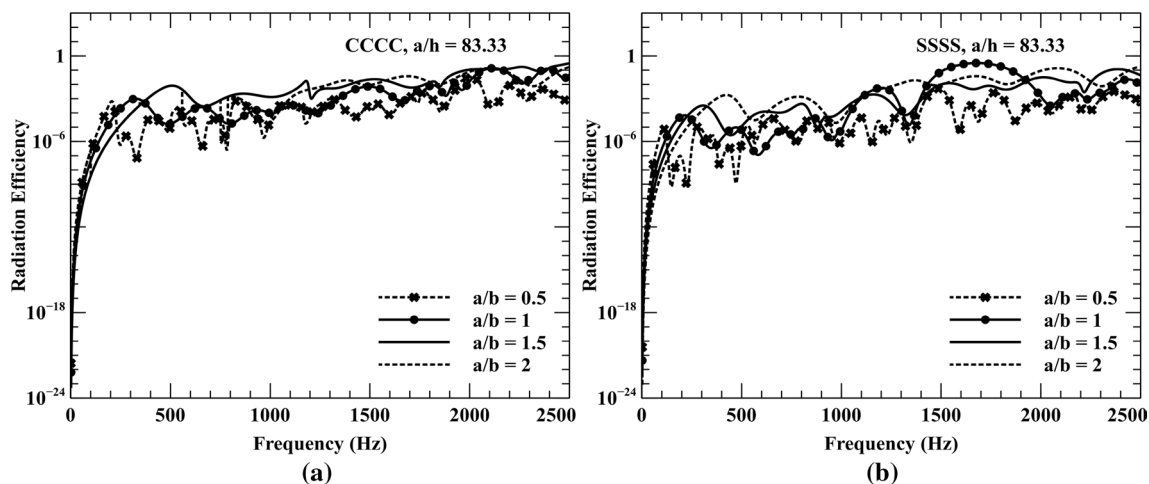


Fig. 17 Effect of radiation efficiency for different aspect ratio and boundary conditions

conditions. Figure 16a and b shows the influence of aspect ratio on average RMS velocity of the GLARE panel for CCCC and SSSS boundary conditions. The results indicate that irrespective of boundary conditions, the curves monotonically have a similar pattern while changing the aspect ratio.

Figure 17a and b shows the results of sound radiation efficiency for CCCC and SSSS boundary conditions. The results indicate that there is no significant variation in radiation efficiency for all cases except the aspect ratio  $a/b = 2$ , which also applies only to CCCC boundary conditions.

The influence of aspect ratio and boundary conditions on radiated sound power level is shown in Fig. 18a and b. It is clear from the figures that at resonant frequencies the radiated sound power level is high, although it is difficult to distinguish the radiated sound power level by just looking at the plot.

The overall sound power level is therefore calculated at 1/3rd Octave band frequency and is useful for differentiating the radiated power for different aspect ratios, as shown in Fig. 15. One can see from Fig. 19a and b that the overall sound power level decreases at 1/3rd octave band frequencies as the aspect ratio of the GLARE panel increases. However, the overall sound power level increases at some octave frequencies for  $a/b = 1$  compared to  $a/b = 0.5$ , which may be due to an increase in natural frequencies as the ratio increases.

The effect of boundary conditions on overall sound power level at 1/3rd Octave band frequencies are plotted as shown in Fig. 19a and b. Figures show that the sound power level decreases while increasing the aspect ratio for all side clamped boundary conditions. However, a similar trend has not been observed for SSSS conditions, as shown in Fig. 19b.

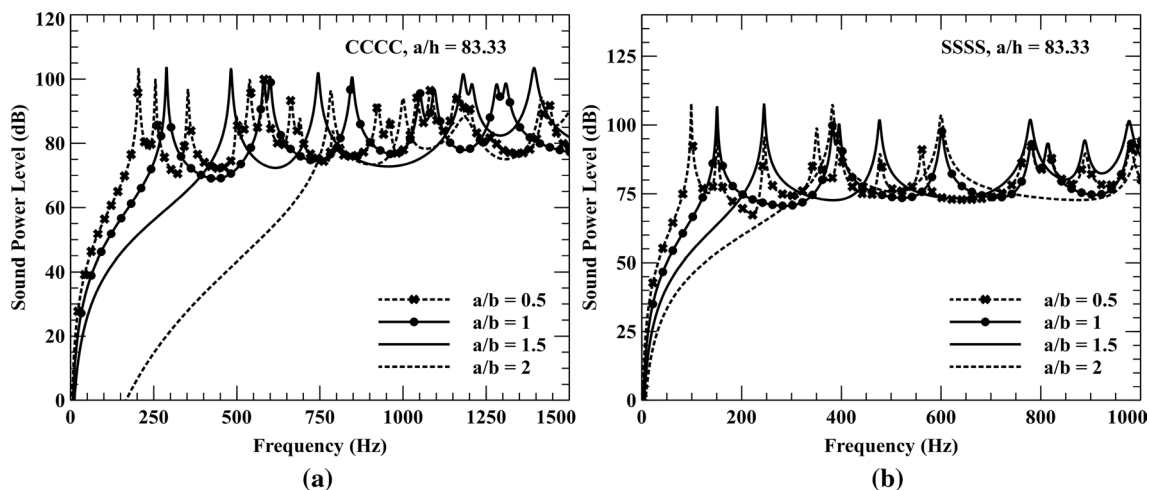


Fig. 18 Effect of sound power level for different aspect ratio and boundary conditions

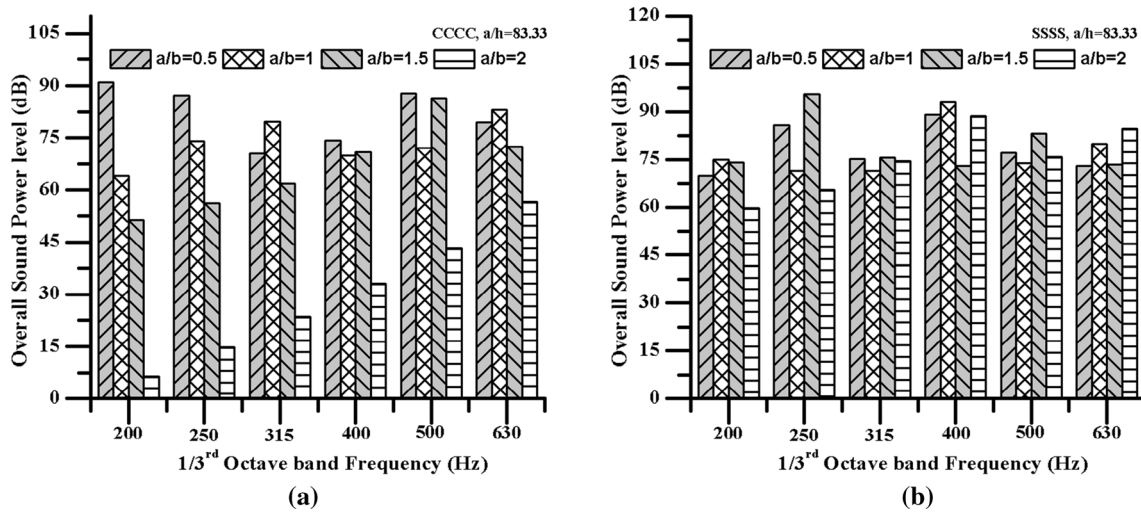


Fig. 19 Effect of aspect ratio and boundary conditions on overall sound power level at 1/3rd octave band frequency

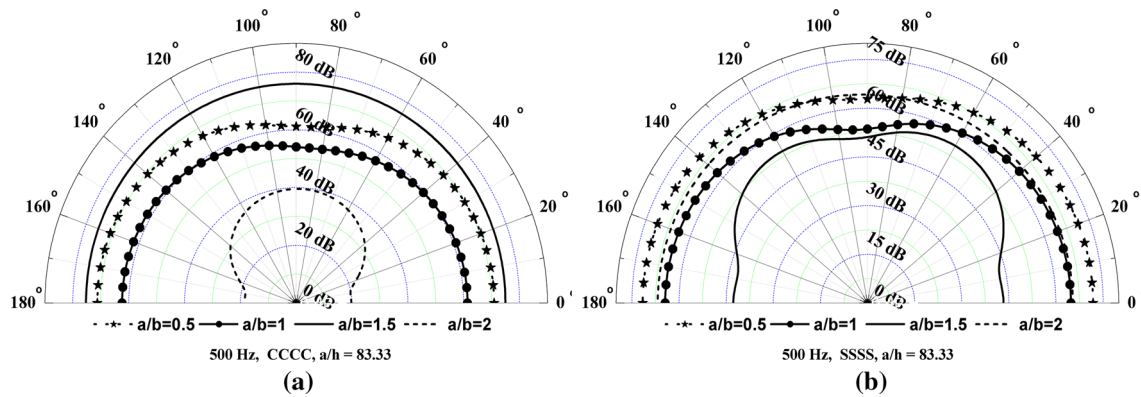


Fig. 20 Effect of sound pressure level at 500 Hz for different aspect ratio with different boundary conditions

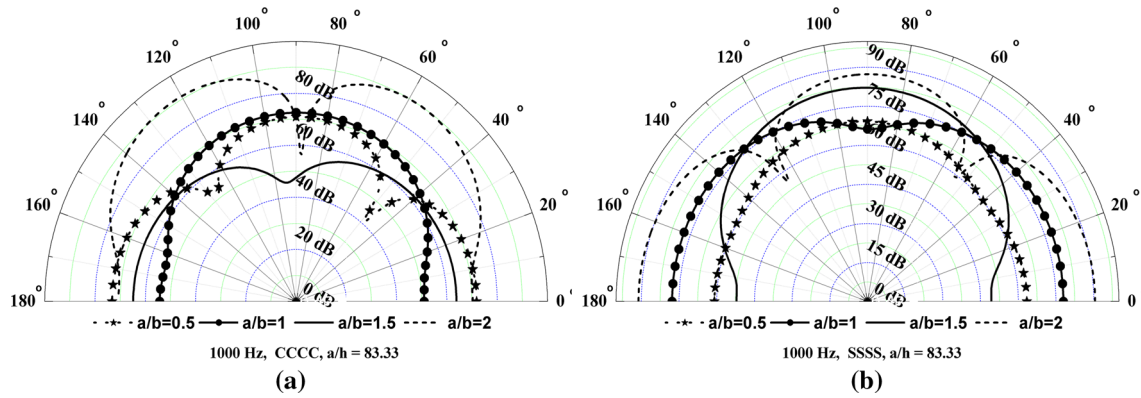


Fig. 21 Effect of sound pressure level at 1000 Hz for different aspect ratio with different boundary conditions

The radiated sound pressure level is calculated by Eq. (34). Figure 20a and b shows the variations in sound directivity pattern due to the change in aspect ratio and boundary conditions for 500 Hz. Figures clearly indicate that the radiated sound pressure level increases as increase in aspect ratio for all side clamped boundary conditions. However, the simply supported boundary conditions do not show much variation for a higher aspect ratio. Figure 21a and b shows the variations in sound directivity pattern due to the change in aspect ratio and boundary conditions for 1000 Hz. The radiated sound pressure level for the CCCC boundary condition shows a definite pattern and represents modes close to 1000 Hz. From Fig. 21a, it is clear that the radiated sound pressure level is not uniform and shows significant variation when increasing the aspect ratio for all side clamped boundary conditions. Irrespective of aspect ratio similar trend has been observed for simply supported boundary conditions as well and the results are shown in Fig. 21b.

Next, the effect of boundary conditions on transmission loss of GLARE-5 panel is examined as specified in Sect. 2.9. A plane acoustic wave with amplitude  $1 \text{ N/m}^2$  and  $0^\circ$  incident angle is considered for analyzing sound transmission loss of the GLARE panel. Figure 22a and b shows the sound transmission loss of all side clamped and simply supported GALRE-5 panel for thickness aspect ratio  $a/h = 83.33$ . From the figures, it is clear that irrespective of boundary conditions, the STL of the panel increases with an increase in aspect ratio.

#### 4.4 Influence of thickness ratio

Vibro-acoustic behavior of the GLARE panel is investigated by varying  $a/h$  ratio for different  $a/b$  ratios. All side clamped boundary conditions with symmetric cross-ply

$[\text{Al}/0^\circ/90^\circ/90^\circ/0^\circ/\text{Al}]_s$  laminate is considered for the detailed investigation. In this analysis, the thickness is maintained based on the manufactured GLARE-5 composite material with 15% of aluminum metal and 85% of composite material. This study's focus is to see how vibration and acoustic characteristics behavior change according to the thickness parameter variation. The fundamental modal frequencies for different thickness ratios along with different aspect ratios are given in Table 9, and it shows that the frequency decreases with an increase in thickness ratio and increases with a decrease in thickness ratio.

Figure 23a and b shows the effect of thickness aspect ratio on average RMS velocity and radiation efficiency of GLARE panel with  $a/b = 1$ . As expected, the modal density is higher for larger thickness aspect ratio and lower for smaller thickness aspect ratio. It is also observed that the radiation efficiency decreases with increase in thickness aspect ratio as shown in Fig. 23b. Similar trends have been observed for  $a/b = 1.5$  and 2 as shown in Figs. 24a, b, 25a and b.

Next, the acoustic response due to the change in aspect ratio is computed using the Rayleigh integral from each nodal velocities corresponding to each excitation frequency. Figure 26a and b shows the radiated sound power level and the overall sound power level of all side clamped GLARE panel at Octave frequencies for  $a/b$  ratio = 1. The variation in sound power level is very similar to the RMS velocity, as expected. The overall sound power level increases as the thickness aspect ratio decrease at a few Octave  $1/3\text{rd}$  frequencies except at 500 Hz, 800 Hz and 100 Hz center frequencies for  $a/h = 83.33$ . This may be due to the increase in modal density at that Octave band region. Similar trends are observed for thickness aspect ratios 1.5 and 2 as shown in Figs. 27a, b, 28a and b.

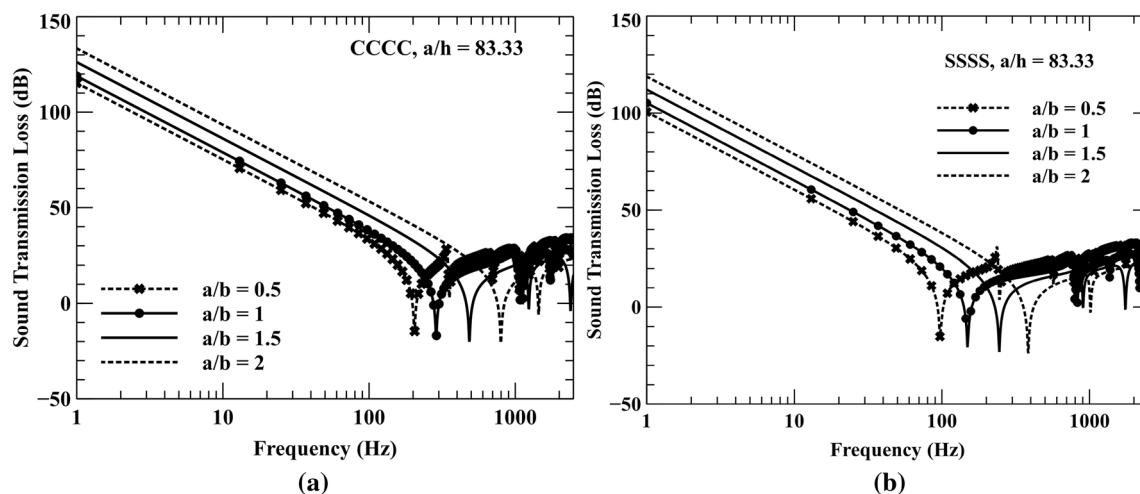
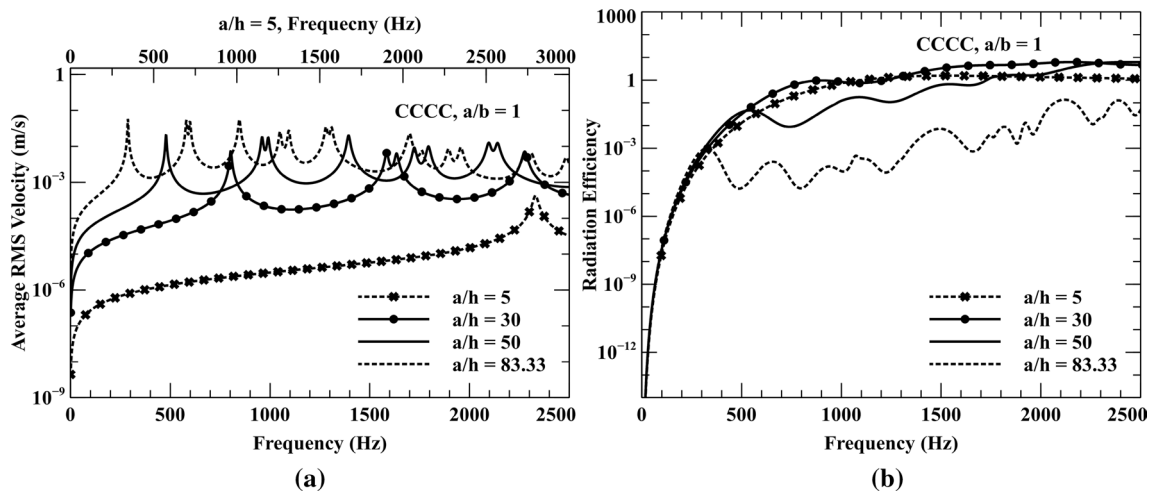


Fig. 22 Effect of sound transmission loss for different aspect ratio with different boundary conditions

**Table 9** Modal frequencies for different thickness ratio with CCCC boundary condition

Boundary conditions	Modal frequencies of GLARE-5 panel (Hz)				
	Mode	$a/h = 5$	$a/h = 30$	$a/h = 50$	$a/h = 83.33$
CCCC $a/b = 1$	1	2797.00	803.37	479.41	288.26
	2	4568.70	1585.50	960.56	580.72
	3	4642.51	1635.11	991.12	599.40
	4	6015.82	2277.10	1394.61	846.69
	5	6817.61	2788.40	1723.92	1050.32
	6	6970.31	2899.31	1794.81	1094.31
CCCC $a/b = 1.5$	1	3831.80	1319.40	798.61	482.67
	2	5351.21	2010.91	1229.00	745.63
	3	6876.71	3087.10	1933.51	1184.00
	4	7462.61	3184.91	1981.41	1210.51
	5	7977.82	3614.51	2275.41	1396.80
	6	8517.81	4569.62	2906.81	1792.70
CCCC $a/b = 2$	1	4984.60	2077.82	1285.22	783.11
	2	6243.90	2634.70	1637.41	999.91
	3	8129.31	3671.81	2308.71	1416.91
	4	9289.71	5032.70	3285.72	2033.90
	5	9566.42	5130.30	3287.31	2048.30
	6	10172	5455.2	3569.72	2228.71



**Fig. 23** Effect of average RMS velocity and radiation efficiency for  $a/b = 1$  with different thickness ratios

The effect of thickness aspect ratio on radiated sound directivity pattern of all side clamped GLARE panel for different aspect ratio at 1500 Hz is shown in Fig. 29a–c. From the figures, it is clear that the radiated sound pressure level increases with an increase in thickness aspect ratio. The variations in sound transmission loss due to the change in thickness aspect ratio for 1500 Hz are shown in Fig. 30a–c. Unlike the aspect ratio  $a/b = 83.333$ , the sound transmission loss of  $a/b = 1, 1.5$  and  $2$  significantly increased for the decrease in thickness aspect ratio. This may be due to the increase in thickness of the GLARE panel.

### 4.5 Influence of material percentage variation

The influence of various percentage combinations of aluminum and GFRC on vibration and acoustic characteristics is studied by considering symmetric cross-ply layout of the all-side clamped GLARE-5 panel. Table 10 shows the free vibration results of the GLARE panel and clearly indicates that the natural frequencies are increasing by adding aluminum with composite material. Therefore, one can select the appropriate Al and GFRC material percentages to fabricate a hybrid multilayered GLARE-5 panel to obtain enhanced vibro-acoustic properties.

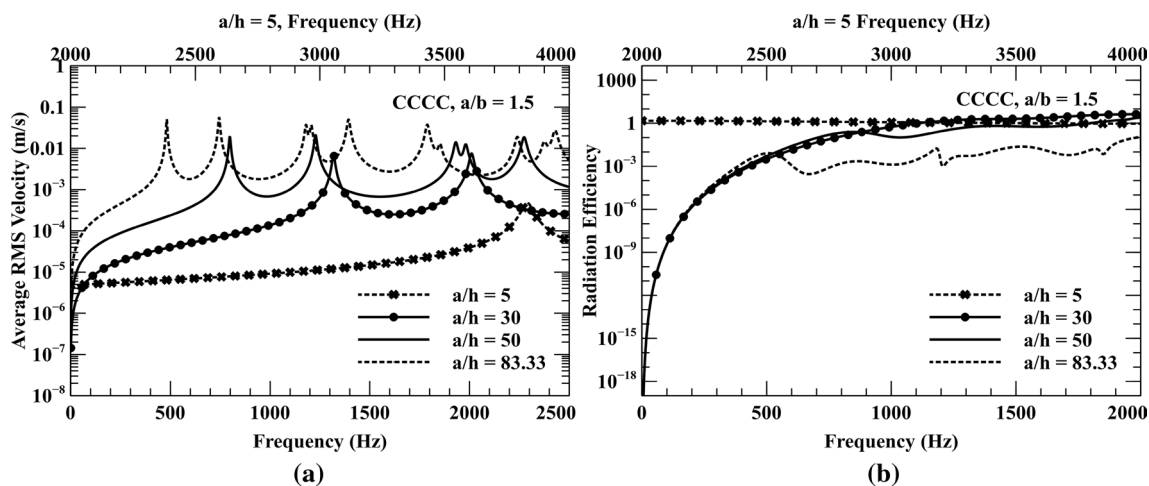


Fig. 24 Effect of average RMS velocity and radiation efficiency for  $a/b = 1.5$  with different thickness ratios

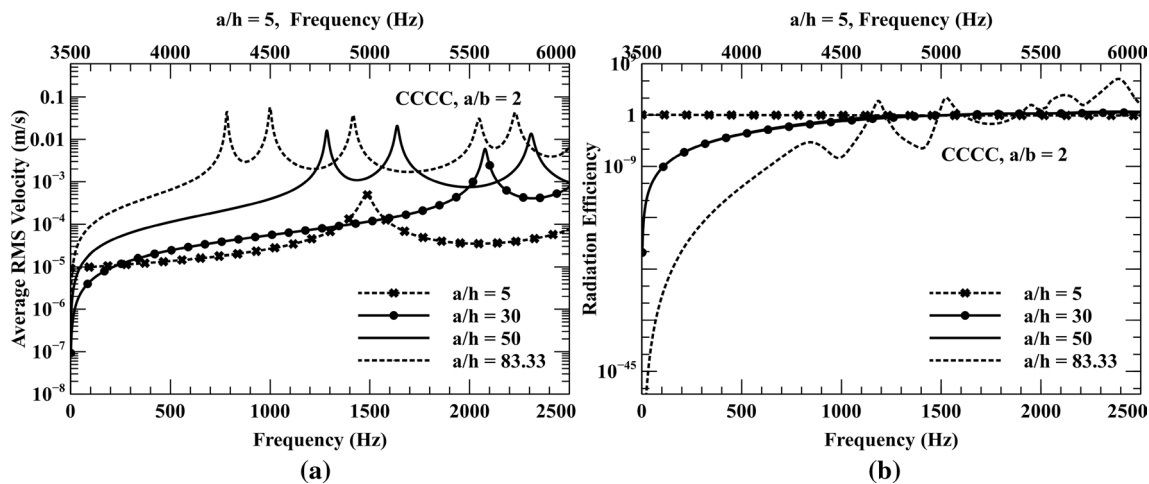


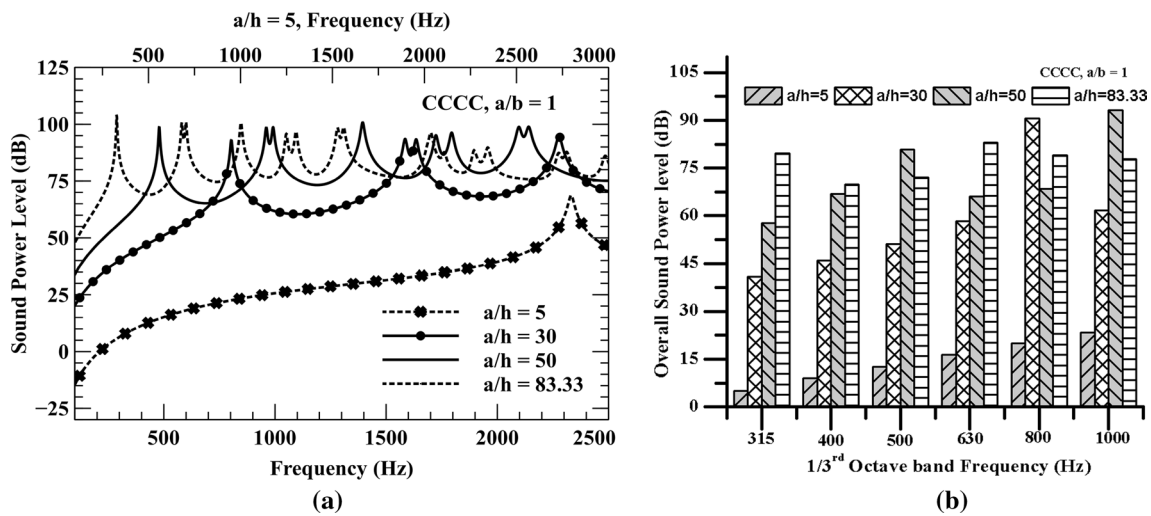
Fig. 25 Effect of average RMS velocity and radiation efficiency for  $a/b = 2$  with different thickness ratios

Figure 31a and b shows the average RMS velocity of the GLARE panel for different material percentage variation along with different thickness ratio  $a/h = 83.33$  and  $a/h = 5$ . The natural frequencies of 100 % GFRC from Fig. 31a are less than 100 % Al and are between GFRC and Al for other configurations. A similar trend is observed for the thick panel as seen in Fig. 31b. Figure 32a and b shows the radiation efficiency of the GALRE panel for different material percentage variation. As shown in the figures, the radiation efficiency shows a significant variation for the thin plate and no variation for the thick plate. The radiated sound power level for different material configurations is shown in Fig. 33a and b. Figures indicate that the radiated sound power level at natural frequencies and show significant variation with respect to the percentage of GFRC and aluminum. Further, the trend for thin and thick GLARE panels does not seem to be different.

Figure 34a and b shows the STL due to change in material percentage variation for thin and thick panels, 100 % Al shows better transmission loss than 100 % GFRC and values for other configurations lie in between them. However, STL for the thin panel does not show much variation if its GFRC percentage is more than 50 %. Therefore, the percentage of GFRC should be kept as low as possible for high STL and at the same time, the percentage should be more than 50 %. This helps to reduce the weight of the GLARE for thin panels without compromising acoustic characteristics.

#### 4.6 Influence of GLARE grades on acoustic characteristics

GLARE panels of different grades are considered to examine sound properties given in Table 1. The radiated sound



**Fig. 26** Effect of sound power level and overall sound power level based on  $1/3^{\text{rd}}$  octave band frequency for  $a/b = 1$  with different thickness ratios

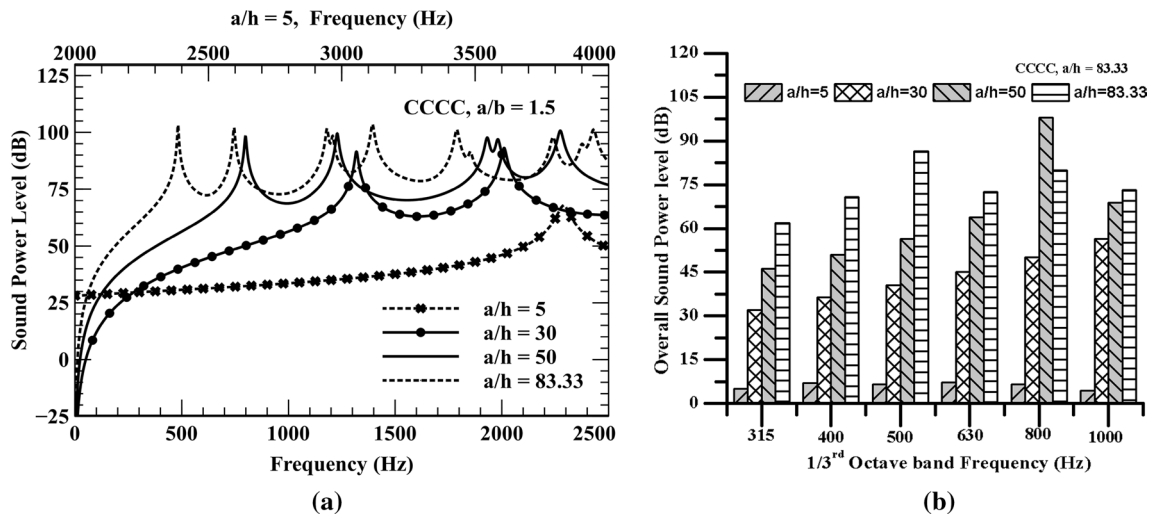


**Fig. 27** Effect of sound power level and overall sound power level based on  $1/3^{\text{rd}}$  octave band frequency for  $a/b = 1.5$  with different thickness ratios

power level and STL are examined for thin and thick plates with  $a/b$  ratios of 1 and 1.5. Figure 35a and b shows the radiated sound power level for square and rectangular thin plates. They indicate that the radiated sound power level does not vary much at the fundamental frequency and show significant variations for higher natural frequencies. Figure 36a and b shows the results of sound transmission loss of various GLARE grades panels. GLARE-4 and GLARE-5 grades exhibit low transmission loss than other grades for both square and rectangular panels. However, the trend does not differ significantly for all other grades.

Similarly, thick GLARE panels with different grades are examined for acoustic characteristics. Figure 37a and b shows the radiated sound power level for square and rectangular thick panels. Unlike thin plates, all thick GLARE grades except GLARE-6 exhibit the same amount of radiated sound power at many resonant frequencies, regardless of the aspect ratio variations. Figure 38a and b shows similar trends in sound transmission loss for square and rectangular thick panels with all grades other than GLARE-4 and GLARE-5. This may be due to the high number of layers associated with GLARE-4 and GLARE-5 when compared to other GLARE grades.

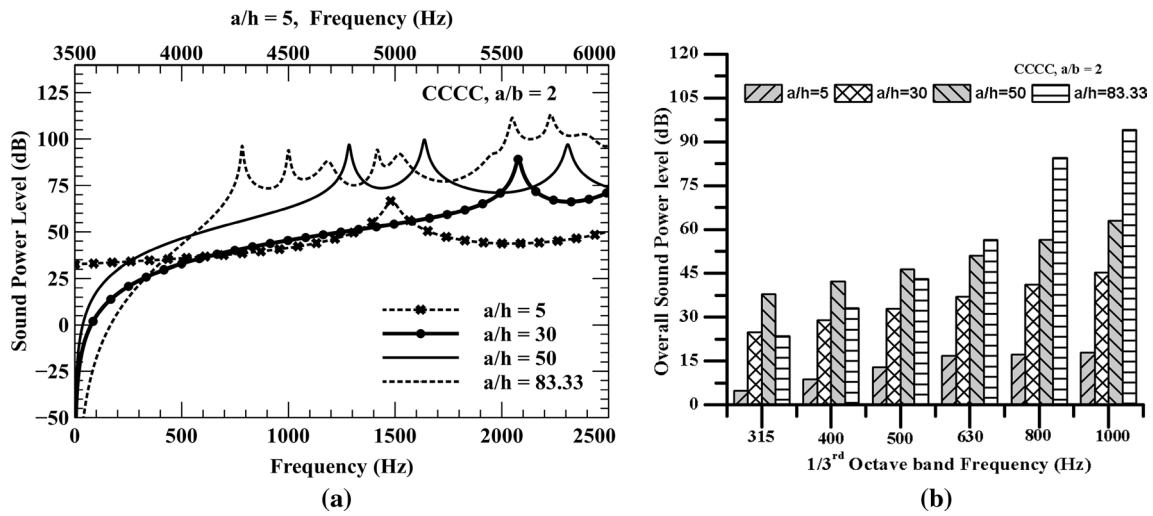


Fig. 28 Effect of sound power level and overall sound power level based on 1/3rd octave band frequency for  $a/b = 2$  with different thickness ratios

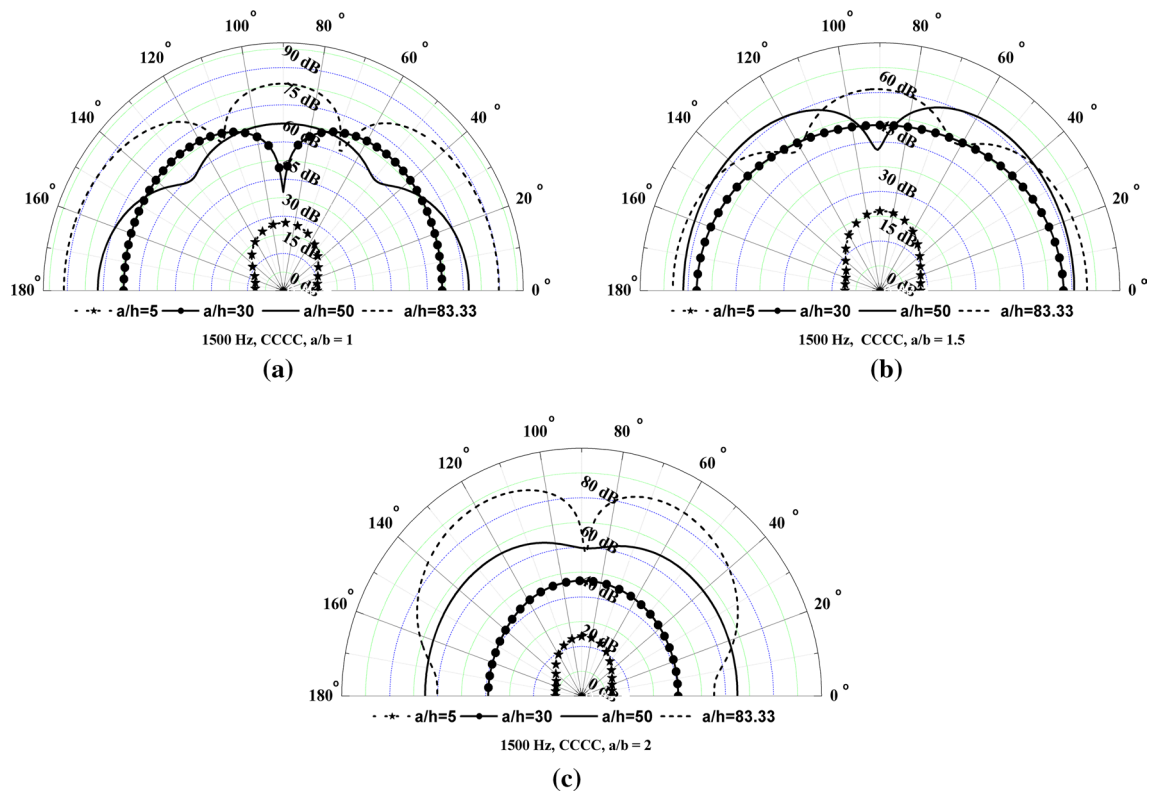


Fig. 29 Effect of sound pressure level at 1500 Hz for different thickness ratios

### 5 Conclusion

In this work, vibro-acoustic characteristic of a hybrid multilayer GLARE-5 composite panel is investigated using experimental and numerical approaches. GLARE-5 panel

with aluminum and unidirectional glass fiber composite are fabricated using the hand layup process. A micromechanics approach was employed to determine the material properties. The free vibration characteristics of the panel are extracted using experimental modal analysis and the results are verified numerically using the finite element approach. Reddy's

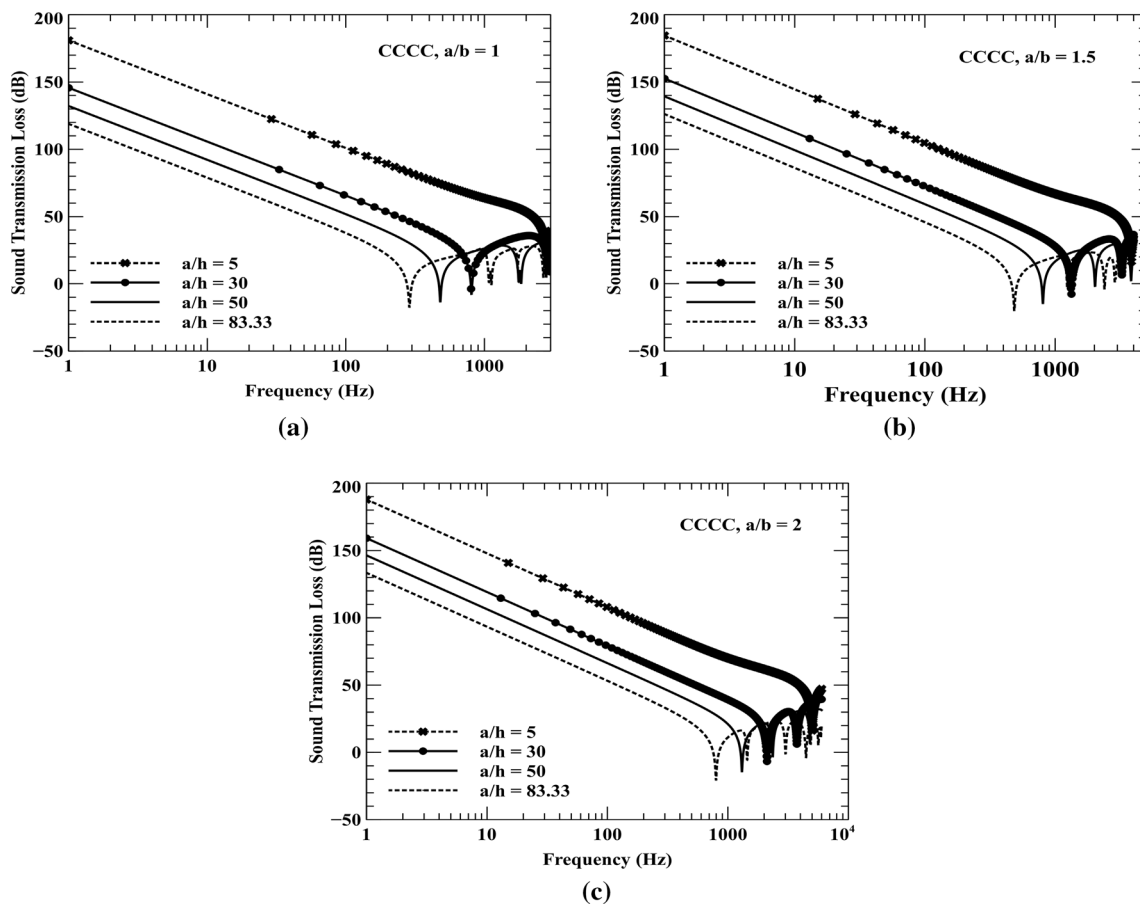


Fig. 30 Effect of sound transmission loss for different thickness ratios

Table 10 Material percentage variation from composite to aluminum

Boundary conditions	Modal frequencies of GLARE-5 panel (Hz)					
	Mode	100% Composite	85% Composite & 15% Al	50% Composite & 50% Al	25% Composite & 75% Al	100% Al
CCCC $alb=1$	1	238.03	288.26	345.41	359.15	362.61
	2	469.91	580.72	703.02	732.30	740.41
	3	509.32	599.40	705.87	732.62	740.41
	4	683.39	846.69	1028.50	1074.51	1090.01
	5	855.20	1050.31	1264.41	1315.01	1331.21
	6	946.92	1094.30	1273.51	1321.61	1337.50

higher-order shear deformation theory based non-confirming finite element was used for this purpose. MAC analysis was carried out to quantify the correlation between experimental and numerical results.

Modal superposition is a method of using the fundamental natural frequencies and mode shapes of the structure from the modal analysis to characterize the dynamic response characteristic of a structure with a steady harmonic

excitation. The Rayleigh integral method is used to get the acoustic properties of the GLARE-5 panel. Vibro-acoustic behavior of GLARE-5 is investigated for different aspect ratios ( $alb$ ), boundary conditions (CCCC & SSSS), thickness aspect ratio ( $a/h$ ), material percentage and GLARE grade variations. Results reveal that irrespective of aspect ratio combination of the low percentage of GFRC with Al exhibits



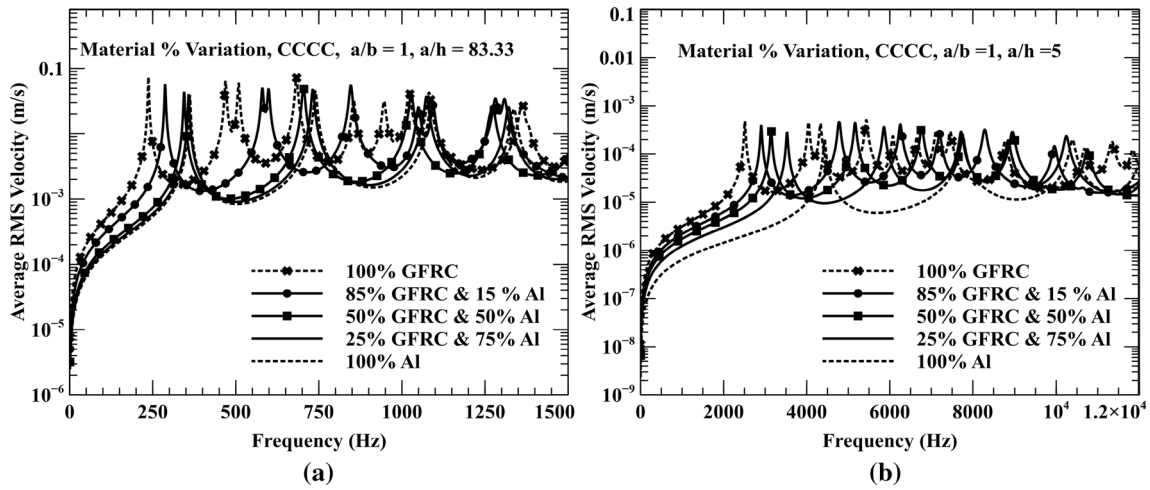


Fig. 31 Effect of average RMS velocity for various material % variation

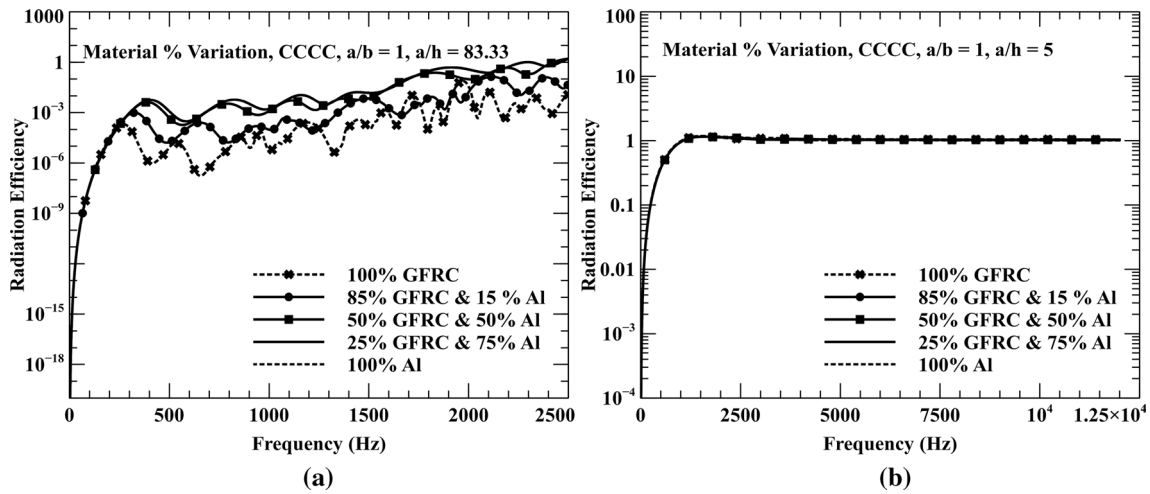


Fig. 32 Effect of radiation efficiency for various material % variation

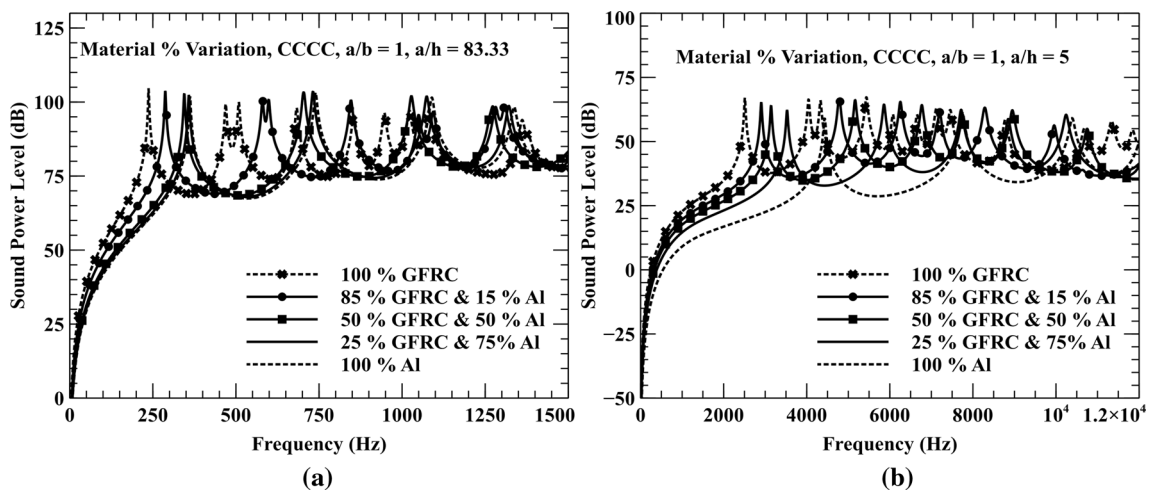


Fig. 33 Effect of sound power level for different material % variation

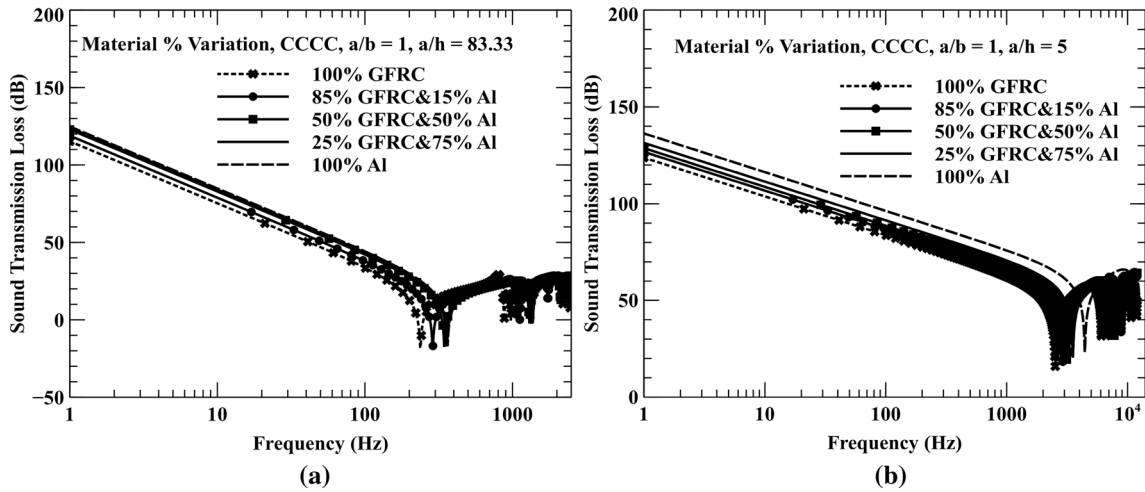


Fig. 34 Effect of sound transmission loss for different material % variation

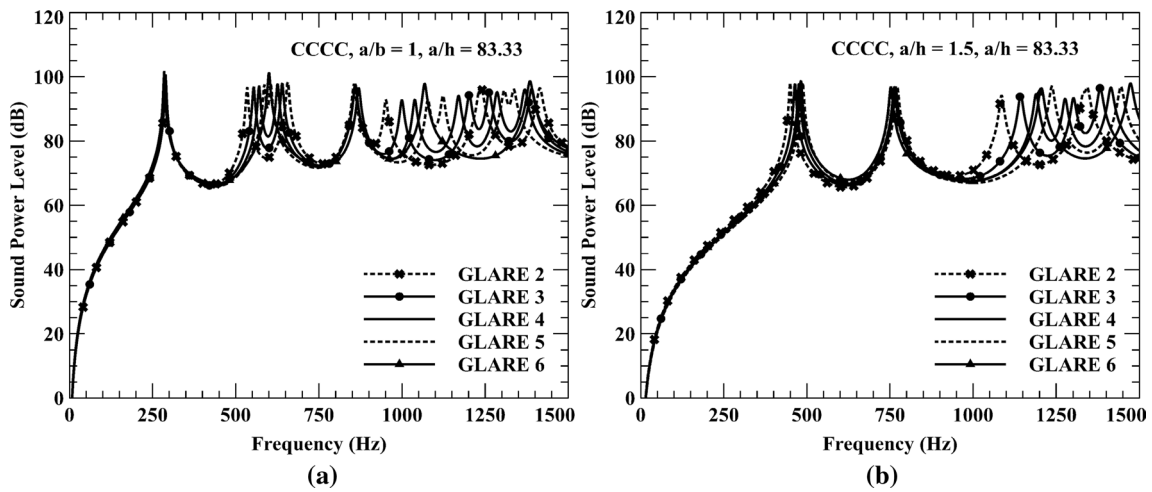


Fig. 35 Effect of sound power level for GLARE grades variation

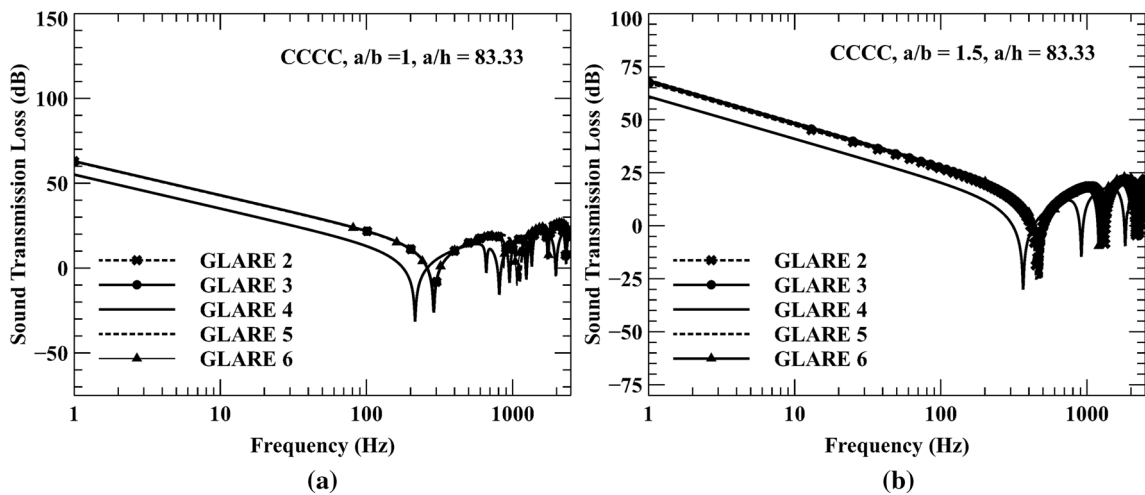


Fig. 36 Effect of sound transmission loss for GLARE grades variation

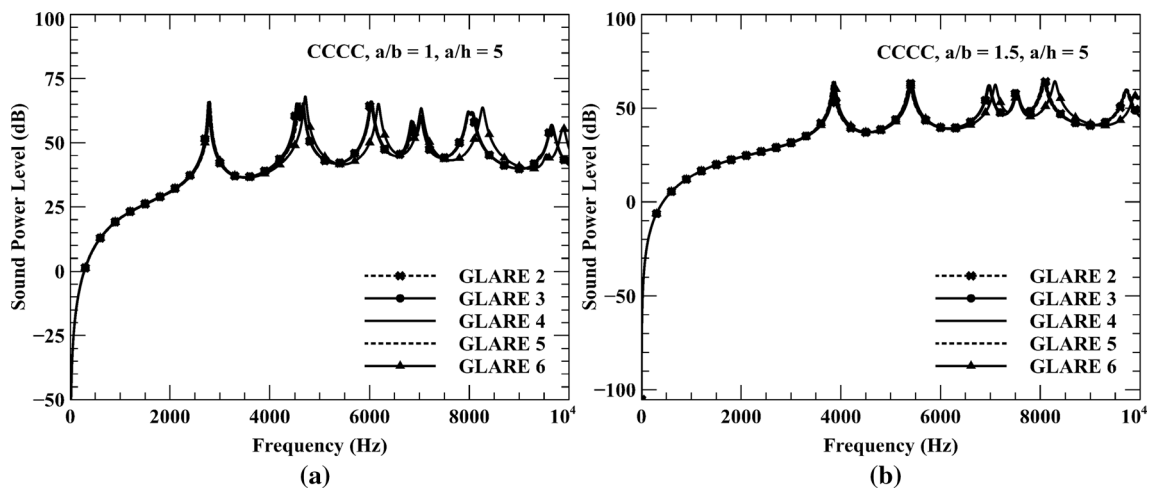


Fig. 37 Effect of sound power level for GLARE grades variation

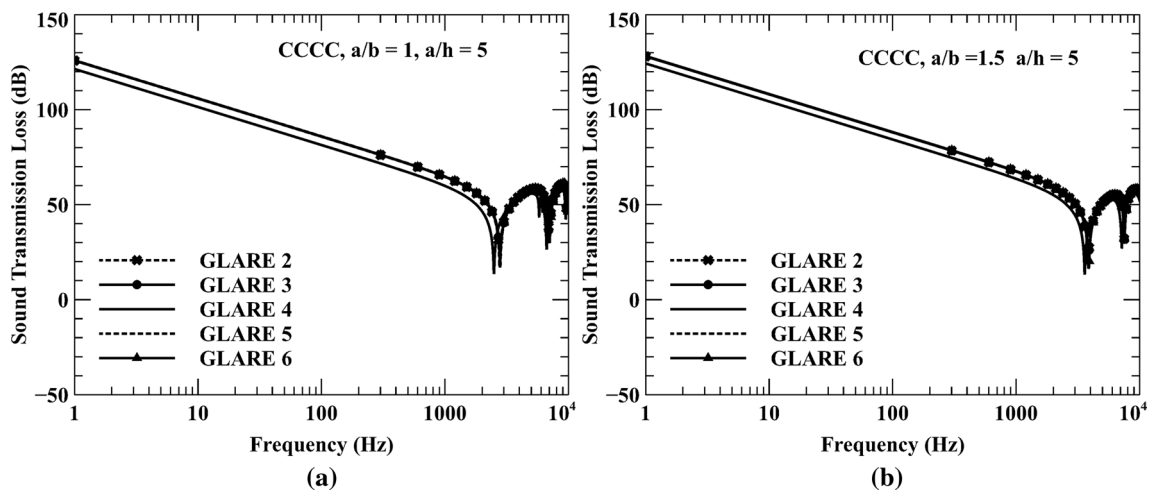


Fig. 38 Effect of sound transmission loss for GLARE grades variation

enhanced vibration and acoustic characteristics than 100 % of GFRC.

The below-mentioned observations were made with respect to vibration and sound response characteristics of GLARE panels:

- Radiated sound power level of thin GLARE panel for CCCC and SSSS boundary conditions shows similar patterns for all aspect ratios. It is clear that the natural frequencies of the GLARE panel shifted to a higher level as the percentage of Al increases, and radiated sound power level showed distinct peaks irrespective of aspect ratios and boundary conditions.
- Irrespective of different aspect ratios, the radiation efficiency of the GLARE panel decreases with an increase in thickness. The radiation efficiency of the thin GLARE panel not varied much for all aspect ratios except all side clamped panel with an aspect ratio ( $a/b$ ) 2. In the same manner, the material percentage variations of all GLARE grades did not show considerable effects on radiation efficiency.
- Thin and thick panels exhibited the same transmission loss for all the GLARE grade variations of GLARE except GLARE-4 and GLARE-5. It was also observed that GLARE-4 and GLARE-5 grades exhibit low transmission loss when compared to other grades for thin/

thick square/rectangular panels. However, the trend does not differ significantly for all other grades. Further, it was found that the transmission loss of the GLARE panel not only depends on thickness but also on the number of composite layers used.

- Irrespective of aspect ratio, combination of the low percentage of GFRC with Al exhibits enhanced vibration and acoustic characteristics than 100 percentage GFRC. Design guidelines for selecting Al and GFRC percentages are provided to obtain enhanced vibro-acoustic properties in hybrid multilayer GLARE panels.

### Appendix

For the conforming elements the nodal values are given by the relations where  $\alpha = 1, 2, 3, 4, 5; \Delta_j^1 = u_j; i = 1$  to  $\alpha$

$$\bar{K}_{ij}^{1\alpha} = \int \left( \frac{\partial \psi_i}{\partial x} \hat{N}_{1j}^{\circ\alpha} + \frac{\partial \psi_i}{\partial y} \hat{N}_{6j}^{\circ\alpha} \right) dx dy,$$

$$\bar{K}_{ij}^{2\alpha} = \int \left( \frac{\partial \psi_i}{\partial x} \hat{N}_{6j}^{\circ\alpha} + \frac{\partial \psi_i}{\partial y} \hat{N}_{2j}^{\circ\alpha} \right) dx dy$$

$$\begin{aligned} \bar{K}_{ij}^{3\alpha} = \int & \left[ \frac{\partial \varphi_i}{\partial x} \hat{Q}_{1j}^{\circ\alpha} + \frac{\partial \varphi_i}{\partial y} \hat{Q}_{2j}^{\circ\alpha} \right. \\ & \left. - c_1 \left( \frac{\partial^2 \varphi_i}{\partial x^2} \hat{P}_{1j}^{\circ\alpha} + 2 \frac{\partial^2 \varphi_i}{\partial x \partial y} \hat{P}_{6j}^{\circ\alpha} \right. \right. \\ & \left. \left. + \frac{\partial^2 \varphi_i}{\partial y^2} \hat{P}_{2j}^{\circ\alpha} \right) \right] dx dy \end{aligned}$$

$$\bar{K}_{ij}^{4\alpha} = \int \left( \frac{\partial \psi_i}{\partial x} \bar{M}_{1j}^{\alpha} + \frac{\partial \psi_i}{\partial y} \bar{M}_{6j}^{\alpha} + \psi_i \hat{Q}_{1j}^{\circ\alpha} \right) dx dy,$$

$$\bar{K}_{ij}^{5\alpha} = \int \left( \frac{\partial \psi_i}{\partial x} \bar{M}_{6j}^{\alpha} + \frac{\partial \psi_i}{\partial y} \bar{M}_{2j}^{\alpha} + \psi_i \hat{Q}_{2j}^{\circ\alpha} \right) dx dy$$

$$\bar{M}_{ij}^{11} = I_0 S_{ij}^0, \bar{M}_{ij}^{12} = 0, \bar{M}_{ij}^{13} = -c_1 I_3 S_{ij}^{\alpha x},$$

$$\bar{M}_{ij}^{14} = J_1 S_{ij}^0, \bar{M}_{ij}^{15} = 0$$

$$\bar{M}_{ij}^{22} = I_0 S_{ij}^0, \bar{M}_{ij}^{23} = -c_1 I_3 S_{ij}^{\alpha y},$$

$$\bar{M}_{ij}^{24} = 0, \bar{M}_{ij}^{25} = J_1 S_{ij}^0$$

$$\bar{M}_{ij}^{33} = I_0 S_{ij}^1 + c_1^2 I_6 \left( S_{ij}^{\alpha x} + S_{ij}^{\alpha y} \right),$$

$$\bar{M}_{ij}^{34} = -c_1 J_4 S_{ji}^{\alpha x}, \bar{M}_{ij}^{35} = c_1 J_4 S_{ji}^{\alpha y}$$

$$\bar{M}_{ij}^{44} = K_2 S_{ij}^0, \bar{M}_{ij}^{45} = 0,$$

$$\bar{M}_{ij}^{55} = K_2 S_{ij}^0$$

$$S_{ij}^{33} = G_{ij}$$

$$= \hat{N}_{xx} \left( S_{ij}^{\alpha y} + S_{ij}^{\alpha x} \right) + \hat{N}_{yy} S_{ij}^{\alpha y}$$

$$\bar{F}_i^1 = \oint_{\Gamma^e} \left( N_{xx} n_x + N_{xy} n_y \right) \psi_i ds,$$

$$\bar{F}_i^2 = \oint_{\Gamma^e} \left( N_{xy} n_x + N_{yy} n_y \right) \psi_i ds$$

$$\bar{F}_i^4 = \oint_{\Gamma^e} \left( M_{xx} n_x + M_{xy} n_y \right) \psi_i ds,$$

$$\bar{F}_i^5 = \oint_{\Gamma^e} \left( M_{xy} n_x + M_{yy} n_y \right) \psi_i ds$$

$$\bar{F}_i^3 = \oint q \varphi_i dx dy + \oint_{\Gamma^e} \left( \bar{V}_n \varphi_i + P_{mn} \frac{\partial \varphi_i}{\partial n} \right) ds$$

$$S_{ij}^0 = \int \psi_i \psi_j dx dy, S_{ij}^{\alpha x} = \int \psi_i \frac{\partial \varphi_j}{\partial x} dx dy,$$

$$S_{ij}^{\alpha y} = \int \psi_i \frac{\partial \varphi_j}{\partial y} dx dy$$

$$S_{ij}^1 = \int \varphi_i \varphi_j dx dy, S_{ij}^{\alpha x} = \int \frac{\partial \varphi_i}{\partial x} \frac{\partial \varphi_j}{\partial x} dx dy,$$

$$S_{ij}^{\alpha y} = \int \frac{\partial \varphi_i}{\partial y} \frac{\partial \varphi_j}{\partial y} dx dy$$

$$N_{1j}^1 = A_{11} \frac{\partial \psi_j}{\partial x} + A_{16} \frac{\partial \psi_j}{\partial y},$$

$$N_{1j}^2 = A_{16} \frac{\partial \psi_j}{\partial x} + A_{12} \frac{\partial \psi_j}{\partial y}$$

$$N_{1j}^3 = -c_1 \left( E_{11} \frac{\partial^2 \varphi_j}{\partial x^2} + 2E_{16} \frac{\partial^2 \varphi_j}{\partial x \partial y} + E_{12} \frac{\partial^2 \varphi_j}{\partial y^2} \right)$$

$$N_{1j}^4 = \hat{B}_{11} \frac{\partial \psi_j}{\partial x} + \hat{B}_{16} \frac{\partial \psi_j}{\partial y},$$

$$N_{1j}^5 = \hat{B}_{12} \frac{\partial \psi_j}{\partial x} + \hat{B}_{16} \frac{\partial \psi_j}{\partial y}$$

$$N_{6j}^1 = A_{16} \frac{\partial \psi_j}{\partial x} + A_{66} \frac{\partial \psi_j}{\partial y},$$

$$N_{6j}^2 = A_{66} \frac{\partial \psi_j}{\partial x} + A_{26} \frac{\partial \psi_j}{\partial y}$$

$$N_{6j}^3 = -c_1 \left( E_{16} \frac{\partial^2 \varphi_j}{\partial x^2} + 2E_{66} \frac{\partial^2 \varphi_j}{\partial x \partial y} + E_{26} \frac{\partial^2 \varphi_j}{\partial y^2} \right)$$

$$N_{6j}^4 = \hat{B}_{66} \frac{\partial \psi_j}{\partial x} + \hat{B}_{16} \frac{\partial \psi_j}{\partial y},$$

$$N_{6j}^5 = \hat{B}_{26} \frac{\partial \psi_j}{\partial x} + \hat{B}_{66} \frac{\partial \psi_j}{\partial y}$$

$$N_{2j}^1 = A_{12} \frac{\partial \psi_j}{\partial x} + A_{26} \frac{\partial \psi_j}{\partial y},$$

$$N_{2j}^2 = A_{26} \frac{\partial \psi_j}{\partial x} + A_{22} \frac{\partial \psi_j}{\partial y}$$

$$N_{2j}^3 = -c_1 \left( E_{12} \frac{\partial^2 \varphi_j}{\partial x^2} + 2E_{26} \frac{\partial^2 \varphi_j}{\partial x \partial y} + E_{22} \frac{\partial^2 \varphi_j}{\partial y^2} \right)$$

$$\begin{aligned}
 N_{2j}^4 &= \hat{B}_{12} \frac{\partial \psi_j}{\partial x} + \hat{B}_{26} \frac{\partial \psi_j}{\partial y}, \\
 N_{2j}^5 &= \hat{B}_{26} \frac{\partial \psi_j}{\partial x} + \hat{B}_{22} \frac{\partial \psi_j}{\partial y} \\
 M_{lj}^1 &= \hat{B}_{11} \frac{\partial \psi_j}{\partial x} + \hat{B}_{16} \frac{\partial \psi_j}{\partial y}, \\
 M_{lj}^2 &= \hat{B}_{16} \frac{\partial \psi_j}{\partial x} + \hat{B}_{12} \frac{\partial \psi_j}{\partial y} \\
 M_{lj}^3 &= -c_1 \left( \hat{F}_{12} \frac{\partial^2 \varphi_j}{\partial x^2} + 2\hat{F}_{16} \frac{\partial^2 \varphi_j}{\partial x \partial y} + \hat{F}_{12} \frac{\partial^2 \varphi_j}{\partial y^2} \right) \\
 \hat{M}_{lj}^4 &= \bar{D}_{11} \frac{\partial \psi_j}{\partial x} + \bar{D}_{16} \frac{\partial \psi_j}{\partial y}, \\
 \hat{M}_{lj}^5 &= \bar{D}_{12} \frac{\partial \psi_j}{\partial x} + \bar{D}_{16} \frac{\partial \psi_j}{\partial y} \\
 \hat{M}_{6j}^1 &= \hat{B}_{16} \frac{\partial \psi_j}{\partial x} + \hat{B}_{66} \frac{\partial \psi_j}{\partial y}, \\
 \hat{M}_{6j}^2 &= \hat{B}_{66} \frac{\partial \psi_j}{\partial x} + \hat{B}_{26} \frac{\partial \psi_j}{\partial y} \\
 M_{6j}^3 &= -c_1 \left( \hat{F}_{16} \frac{\partial^2 \varphi_j}{\partial x^2} + 2\hat{F}_{66} \frac{\partial^2 \varphi_j}{\partial x \partial y} + \hat{F}_{26} \frac{\partial^2 \varphi_j}{\partial y^2} \right) \\
 \hat{M}_{6j}^4 &= \bar{D}_{16} \frac{\partial \psi_j}{\partial x} + \bar{D}_{66} \frac{\partial \psi_j}{\partial y}, \\
 \hat{M}_{6j}^5 &= \bar{D}_{26} \frac{\partial \psi_j}{\partial x} + \bar{D}_{66} \frac{\partial \psi_j}{\partial y} \\
 \hat{M}_{2j}^1 &= \hat{B}_{12} \frac{\partial \psi_j}{\partial x} + \hat{B}_{26} \frac{\partial \psi_j}{\partial y}, \\
 \hat{M}_{2j}^2 &= \hat{B}_{26} \frac{\partial \psi_j}{\partial x} + \hat{B}_{22} \frac{\partial \psi_j}{\partial y} \\
 M_{2j}^3 &= -c_1 \left( \hat{F}_{12} \frac{\partial^2 \varphi_j}{\partial x^2} + 2\hat{F}_{26} \frac{\partial^2 \varphi_j}{\partial x \partial y} + \hat{F}_{22} \frac{\partial^2 \varphi_j}{\partial y^2} \right) \\
 \hat{M}_{2j}^4 &= \bar{D}_{12} \frac{\partial \psi_j}{\partial x} + \bar{D}_{26} \frac{\partial \psi_j}{\partial y}, \\
 \hat{M}_{2j}^5 &= \bar{D}_{22} \frac{\partial \psi_j}{\partial x} + \bar{D}_{26} \frac{\partial \psi_j}{\partial y}
 \end{aligned}$$

$$\begin{aligned}
 P_{lj}^1 &= E_{11} \frac{\partial \psi_j}{\partial x} + E_{16} \frac{\partial \psi_j}{\partial y}, \\
 P_{lj}^2 &= E_{12} \frac{\partial \psi_j}{\partial x} + E_{16} \frac{\partial \psi_j}{\partial y} \\
 P_{lj}^3 &= -c_1 \left( H_{11} \frac{\partial^2 \varphi_j}{\partial x^2} + 2H_{16} \frac{\partial^2 \varphi_j}{\partial x \partial y} + H_{12} \frac{\partial^2 \varphi_j}{\partial y^2} \right) \\
 P_{lj}^4 &= \hat{F}_{11} \frac{\partial \psi_j}{\partial x} + \hat{F}_{16} \frac{\partial \psi_j}{\partial y}, \\
 P_{lj}^5 &= \hat{F}_{12} \frac{\partial \psi_j}{\partial x} + \hat{F}_{16} \frac{\partial \psi_j}{\partial y} \\
 P_{2j}^1 &= E_{12} \frac{\partial \psi_j}{\partial x} + E_{26} \frac{\partial \psi_j}{\partial y}, \\
 P_{2j}^2 &= E_{22} \frac{\partial \psi_j}{\partial x} + E_{26} \frac{\partial \psi_j}{\partial y} \\
 P_{2j}^3 &= -c_1 \left( H_{21} \frac{\partial^2 \varphi_j}{\partial x^2} + 2H_{26} \frac{\partial^2 \varphi_j}{\partial x \partial y} + H_{22} \frac{\partial^2 \varphi_j}{\partial y^2} \right) \\
 P_{2j}^4 &= \hat{F}_{12} \frac{\partial \psi_j}{\partial x} + \hat{F}_{26} \frac{\partial \psi_j}{\partial y}, \\
 P_{2j}^5 &= \hat{F}_{22} \frac{\partial \psi_j}{\partial x} + \hat{F}_{26} \frac{\partial \psi_j}{\partial y} \\
 P_{6j}^1 &= E_{16} \frac{\partial \psi_j}{\partial x} + E_{66} \frac{\partial \psi_j}{\partial y}, \\
 P_{6j}^2 &= E_{26} \frac{\partial \psi_j}{\partial x} + E_{66} \frac{\partial \psi_j}{\partial y} \\
 P_{6j}^3 &= -c_1 \left( H_{16} \frac{\partial^2 \varphi_j}{\partial x^2} + 2H_{66} \frac{\partial^2 \varphi_j}{\partial x \partial y} + H_{26} \frac{\partial^2 \varphi_j}{\partial y^2} \right) \\
 P_{6j}^4 &= \hat{F}_{16} \frac{\partial \psi_j}{\partial x} + \hat{F}_{66} \frac{\partial \psi_j}{\partial y}, \\
 P_{6j}^5 &= \hat{F}_{26} \frac{\partial \psi_j}{\partial x} + \hat{F}_{66} \frac{\partial \psi_j}{\partial y}
 \end{aligned}$$

$$\hat{Q}_{1j}^3 = \bar{A}_{55} \frac{\partial \varphi_j}{\partial x} + \bar{A}_{45} \frac{\partial \varphi_j}{\partial y},$$

$$\hat{Q}_{2j}^3 = \bar{A}_{45} \frac{\partial \varphi_j}{\partial x} + \bar{A}_{44} \frac{\partial \varphi_j}{\partial y}$$

$$\hat{Q}_{1j}^4 = \hat{A}_{55} \varphi_j, \hat{Q}_{1j}^5 = \hat{Q}_{2j}^4 = \hat{A}_{45} \varphi_j,$$

$$\hat{Q}_{2j}^5 = \hat{A}_{44} \varphi_j$$

$$F_i^1 = \oint_{\Gamma^e} \varphi_i N_n ds, F_i^2 = \oint_{\Gamma^e} \varphi_i N_{ns} ds$$

$$F_i^4 = \oint_{\Gamma^e} \varphi_i M_n ds, F_i^5 = \oint_{\Gamma^e} \varphi_i M_{ns} ds$$

$$F_i^3 = \oint_{\Gamma^e} q \varphi_i dx dy + \oint_{\Gamma^e} \varphi_i Q_n ds$$

**Single Isotropic Layer**

$$A_{11} = \frac{Eh}{1 - \nu^2}, A_{12} = \nu A_{11}, A_{22} = A_{11},$$

$$A_{66} = \frac{1 - \nu}{2} A_{11}, A_{44} = A_{55} = \frac{1 - \nu}{2} A_{11}$$

$$D_{11} = \frac{Eh^3}{12(1 - \nu^2)}, D_{12} = \nu D_{11}, D_{22} = D_{11},$$

$$D_{66} = \frac{1 - \nu}{2} D_{11}$$

**Single Specially Orthotropic Layer**

$$A_{11} = Q_{11}h, A_{12} = Q_{12}h, A_{22} = Q_{22}h$$

$$A_{66} = Q_{66}h, A_{44} = Q_{44}h, A_{55} = Q_{55}h$$

$$D_{11} = \frac{Q_{11}h^3}{12}, D_{12} = \frac{Q_{12}h^3}{12}, D_{22} = \frac{Q_{22}h^3}{12}, D_{66} = \frac{Q_{66}h^3}{12}$$

$$F_{11} = \frac{Q_{11}h^5}{80}, F_{12} = \frac{Q_{12}h^5}{80}, F_{22} = \frac{Q_{22}h^5}{80}, F_{66} = \frac{Q_{66}h^5}{80}$$

$$H_{11} = \frac{Q_{11}h^7}{448}, H_{12} = \frac{Q_{12}h^7}{448},$$

$$H_{22} = \frac{Q_{22}h^7}{448}, H_{66} = \frac{Q_{66}h^7}{448}$$

$$Q_{11} = \frac{E_1}{1 - \nu_{12}\nu_{21}}, Q_{12} = \frac{\nu_{12}E_2}{1 - \nu_{12}\nu_{21}} = \frac{\nu_{21}E_2}{1 - \nu_{12}\nu_{21}},$$

$$Q_{22} = \frac{E_2}{1 - \nu_{12}\nu_{21}}$$

$$Q_{66} = G_{12}, Q_{44} = G_{23}, Q_{55} = G_{13}$$

$$\bar{Q}_{11} = Q_{11} \cos^4 \theta + 2(Q_{12} + 2Q_{66}) \sin^2 \theta \cos^2 \theta + Q_{22} \sin^4 \theta$$

$$\bar{Q}_{12} = (Q_{11} + Q_{22} - 4Q_{66}) \sin^2 \theta \cos^2 \theta + Q_{12} (\sin^4 \theta + \cos^4 \theta)$$

$$\bar{Q}_{22} = Q_{11} \sin^4 \theta + 2(Q_{12} + 2Q_{66}) \sin^2 \theta \cos^2 \theta + Q_{22} \cos^4 \theta$$

$$\bar{Q}_{16} = (Q_{11} - Q_{12} - 2Q_{66}) \sin \theta \cos^3 \theta + (Q_{12} - Q_{22} + 2Q_{66}) \sin^3 \theta + \cos \theta$$

$$\bar{Q}_{26} = (Q_{11} - Q_{12} - 2Q_{66}) \sin^3 \theta \cos \theta + (Q_{12} - Q_{22} + 2Q_{66}) \sin \theta + \cos^3 \theta$$

$$\bar{Q}_{66} = (Q_{11} + Q_{22} - 2Q_{12} - 2Q_{66}) \sin^2 \theta \cos^2 \theta + Q_{66} (\sin^4 \theta + \cos^4 \theta)$$

$$\alpha_{xx} = \alpha_1 \cos^2 \theta + \alpha_2 \sin^2 \theta$$

$$\alpha_{yy} = \alpha_1 \sin^2 \theta + \alpha_2 \cos^2 \theta$$

$$2\alpha_{xy} = 2(\alpha_1 - \alpha_2) \sin \theta + \cos \theta$$

$$c_1 = \frac{4}{3h^2}, c_3 = \frac{3}{4h}, c_4 = \frac{5}{3h^2}, f(z) = z(1 - c_1 z^2)$$

$$\hat{A}_{ij} = A_{ij} - c_1 D_{ij}, \hat{B}_{ij} = B_{ij} - c_1 E_{ij},$$

$$\hat{D}_{ij} = D_{ij} - c_1 F_{ij} (i, j = 1, 2, 6)$$

$$\hat{F}_{ij} = F_{ij} - c_1 H_{ij},$$

$$\bar{A}_{ij} = \hat{A}_{ij} - c_1 \hat{D}_{ij} = A_{ij} - 2c_1 D_{ij} + c_1^2 F_{ij} (i, j = 1, 2, 6)$$

$$\bar{D}_{ij} = \hat{D}_{ij} - c_1 \hat{F}_{ij} = D_{ij} - 2c_1 F_{ij} + c_1^2 H_{ij} (i, j = 1, 2, 6)$$

$$\bar{A}_{ij} = \hat{A}_{ij} - c_2 \hat{D}_{ij} = A_{ij} - 2c_2 D_{ij} + c_2^2 F_{ij} (i, j = 4, 5)$$

**Lagrangian interpolation for modeling plate**

$$N_i = \frac{1}{4} (1 + \xi \xi_i) (1 + \eta \eta_i)$$

**References**

1. Sinmazcelik T, Avcu E, Bora MO, Coban O (2011) A review: fibre metal laminates, background, bonding types and applied test methods. *Mater Des* 32(7):3671–3685
2. Gunnink JW, Vlot A, de Vries TJ, van der Hoeven W (2002) Glare technology development 1997–2000. *Appl Compos Mater* 9(4):201–219 (ISSN 1573-4897)
3. Vlot A, Gunnink JW (2011) Fibre metal laminates: an introduction. Springer, Berlin
4. Holleman E (1994) Glare development—an overview. Delft University of Technology, Delft
5. Sinke J (2003) Manufacturing of glare parts and structures. *Appl Compos Mater* 10(4):293–305
6. Botelho EC, Silva RA, Pardini LC, Rezende MC (2006) A review on the development and properties of continuous fiber/epoxy/aluminum hybrid composites for aircraft structures. *Mater Res* 9:247–256
7. Guocai W, Yang JM (2005) The mechanical behavior of GLARE laminates for aircraft structures. *JOM* 57(1):72–79
8. Wilk MS, Sliwa RE (2024) The influence of features of aluminium alloys, 6061 and 7075 on the properties of glare-type composites. *Arch Metall Mater* 60:2015
9. Ardakani MA, Khatibi AA, Ghazavi SA (2008) A study on the manufacturing of Glass-Fiber-Reinforced Aluminum Laminates and the effect of interfacial adhesive bonding on the impact behavior. In: Proceedings of the XIth international congress and exposition. Society for Experimental Mechanics Inc, Florida USA
10. Sadighi M, Pärnänen T, Alderliesten RC, Sayeafatabi M, Benedictus R (2011) Experimental and numerical investigation of metal type and thickness effects on the impact resistance of fiber metal laminates. *Appl Compos Mater* 19(3–4):545–559
11. Hinz S, Jones FR, Schulte K (2007) Micromechanical modelling of shear deformation of a ply 90° in glare at elevated temperatures. *Comput Mater Sci* 39(1):142–148

12. Chen D, Cheng S (1993) Analysis of composite materials: a micro-mechanical approach. *J Reinf Plast Compos* 12(12):1323–1338
13. Chen D, Cheng S (1995) A micromechanical analysis of the elastic behavior of aligned short-fiber reinforced composites. *J Reinf Plast Compos* 14(4):333–348
14. Chen J, Sun C (1988) Modeling of orthotropic elastic-plastic properties of ARALL laminates. In: 29th structures, structural dynamics and materials conference. American Institute of Aeronautics and Astronautics
15. Wang ASD (1999) Micromechanics analysis of composite materials. In: Soares CAM, Soares CMM, Freitas MJM (eds) *Mechanics of composite materials and structures*. NATO science series, vol 361. Springer, Dordrecht, pp 81–130
16. Upadhyay PC, Lyons JS (2008) Elastic constants of uniaxially fiber-reinforced composites with degraded interphase. *J Reinf Plast Compos* 28(12):1441–1458
17. Soltani P, Keikhosravi M, Oskouei RH, Soutis C (2010) Studying the tensile behaviour of GLARE laminates: a finite element modelling approach. *Appl Compos Mater* 18(4):271–282
18. Lee B-E, Park T, Kim J, Kang B-S, Song W-J (2013) Investigation on the tensile behavior of fiber metal laminates based on self-reinforced polypropylene. In: AIP
19. Harras B (2002) Investigation of non-linear free vibrations of fully clamped symmetrically laminated carbon-fibre-reinforced PEEK (AS4/APC2) rectangular composite panels. *Compos Sci Technol* 62(5):719–727
20. Botelho EC, Campos AN, de Barros E, Pardini LC, Rezende MC (2005) Damping behavior of continuous fiber/metal composite materials by the free vibration method. *Compos Part B Eng* 37(2–3):255–263
21. Rahimi GH, Gazor MS, Hemmatnezhad M, Toorani H (2014) Free vibration analysis of fiber metal laminate annular plate by state-space based differential quadrature method. *Adv Mater Sci Eng* 2014:1–11
22. Heylen W, Janter T (1990) Extensions of the modal assurance criterion. *J Vib Acoust* 112(4):468–472
23. Allemang RJ (2003) The modal assurance criterion—twenty years of use and abuse. *Sound Vib* 37(8):14–23
24. Rayleigh L (1984) *The theory of sound*. McMillan and Co., London
25. Li S, Li X (2008) The effects of distributed masses on acoustic radiation behavior of plates. *Appl Acoust* 69(3):272–279
26. Chandra N, Raja S, Nagendra Gopal KV (2014) Vibro-acoustic response and sound transmission loss analysis of functionally graded plates. *J Sound Vib* 333(22):5786–5802
27. Sharma N, Mahapatra TR, Panda SK (2017) Vibro-acoustic behaviour of shear deformable laminated composite flat panel using BEM and the higher order shear deformation theory. *Compos Struct* 180:116–129
28. Arunkumar MP, Jagadeesh M, Pitchaimani J, Gangadharan KV, Lenin Babu MC (2016) Sound radiation and transmission loss characteristics of a honeycomb sandwich panel with composite facings: effect of inherent material damping. *J Sound Vib* 383:221–232
29. Arunkumar MP, Pitchaimani J, Gangadharan KV, Leninbabu MC (2018) Vibro-acoustic response and sound transmission loss characteristics of truss core sandwich panel filled with foam. *Aerosp Sci Technol* 78:1–11
30. Doong J-L, Chen T-J, Chen L-W (1987) Vibration and stability of an initially stressed laminated plate based on a higher-order deformation theory. *Compos Struct* 7(4):285–309
31. Khoa NN, Thinh TI (2007) Finite element analysis of laminated composite plates using high order shear deformation theory. *Vietnam J Mech* 29(1):47–57
32. Sharma N, Mahapatra TR, Panda SK, Hirwani CK (2018) Acoustic radiation and frequency response of higher-order shear deformable multilayered composite doubly curved shell panel—an experimental validation. *Appl Acoust* 133:38–51
33. Hoa SV (2009) *Principles of the manufacturing of composite materials*. DEStech Publications Inc, Lancaster
34. Harras B, Benamar R, White RG (2002) Experimental and theoretical investigation of the linear and non-linear dynamic behaviour of a glare 3 hybrid composite panel. *J Sound Vib* 252(2):281–315
35. Barbero EJ (2017) *Introduction to composite materials design*. CRC Press, Boca Raton
36. Jones RM (2014) *Mechanics of composite materials*. CRC Press, Boca Raton
37. Reddy JN (2003) *Mechanics of laminated composite plates and shells: theory and analysis*. CRC Press, Boca Raton
38. Pastor M, Binda M, Harčarik T (2012) Modal assurance criterion. *Proc Eng* 48:543–548
39. Jeyaraj P, Padmanabhan C, Ganesan N (2008) Vibration and acoustic response of an isotropic plate in a thermal environment. *ASME J Vib Acoust* 130(5):051005
40. Lihui X, Ma M (2020) Study of the characteristics of train-induced dynamic SIFS of tunnel lining cracks based on the modal superposition approach. *Eng Fract Mech* 233:107069
41. Roussos LA (1984) Noise transmission loss of a rectangular plate in an infinite baffle. *J Acoust Soc Am* 75(S1):S2–S3
42. Shi P, Dong C, Sun F, Liu W, Qiankun H (2018) A new higher order shear deformation theory for static, vibration and buckling responses of laminated plates with the isogeometric analysis. *Compos Struct* 204:342–358

**Publisher's Note** Springer Nature remains neutral with regard to jurisdictional claims in published maps and institutional affiliations.